Nonlinear Dyn (2025) 113:23999–24019
https://doi.org/10.1007/s11071-024-10724-6

RESEARCH

Band evolution and 2D nonreciprocal wave propagation in strongly nonlinear meta-plates

Chen Gong · Xin Fang · Li Cheng

Received: 29 July 2024 / Accepted: 25 November 2024 / Published online: 30 December 2024

Abstract Nonlinear meta-materials/structures can enable exotic wave phenomena, leading to extraordinary functionalities, but the bandgap properties and nonreciprocal wave manipulation in high-dimensional nonlinear metamaterials, such as plates, are not fully understood. In this study, we examine the band evolution and nonreciprocal wave propagation in a two-dimensional (2D) strongly nonlinear meta-plate based on analytical methods and numerical integration on the infinite model. The 2D dispersion curves are obtained through combining harmonic balance and Shooting-Newton iteration methods. Numerical studies show that the 2D nonlinear meta-plate exhibits band degeneration and self-adaptive propagation, analogous to 1D cases. However, as confirmed analytically, both band degeneration and self-adaptivity are regulated by the spatial wave divergence in the 2D meta-plate. Furthermore, combining nonlinear and linear portions of a meta-plate entails nonreciprocal wave propagation in 2D space with elucidated physical properties and mechanisms specific to 2D wave propagation. In light of the above, this work presents new computational methods as well as the elucidation of new wave phenomena and properties which are conducive to wave manipulation in 2D strongly nonlinear meta-materials/structures.

Keywords Strongly nonlinear meta-materials/structures · Self-adaptivity · Band degeneration · Nonreciprocity

C. Gong · L. Cheng (✉)
Department of Mechanical Engineering, Hong Kong Polytechnic University, Hung Hom, Kowloon 999077, Hong Kong
e-mail: li.cheng@polyu.edu.hk

X. Fang (✉)
Laboratory of Science and Technology On Integrated Logistics Support, College of Intelligent Science and Technology, National University of Defense Technology, Changsha 410073, Hunan, China
e-mail: xinfangdr@sina.com

1 Introduction

Acoustic metamaterials (AMs) are artificial structures characterized by subwavelength properties [1–4], which are predominantly characterized by their bandgaps. Owing to effectively elastic wave attenuation, bandgaps provide meaningful ways for vibration reduction [5–8]. Nonlinear acoustic metamaterials (NAMs) [9] have gained increasing attention due to their extraordinary properties, vast potential applications as well as extreme scientific interests. For instance, they have been shown to achieve ultralow-frequency and ultrabroad band wave attenuation, surpassing the bandwidth limit of linear counterpart [10, 11], and entail vibration and acoustic reduction in ultralow and ultrabroad frequency [12, 13] etc.

Numerous studies have attempted to comprehend the nonlinear band structures of NAMs, seeking to break the barriers set by linear elasticity [14–16]. The Bragg and local resonant bandgaps in NAMs are amplitude-dependent [17–21]. A primary challenge arising from the amplitude-dependent feature concerns the methodology for predicting band structures. Existing analysis methods include the perturbation method [16, 17, 22–25], the harmonic balance method [12, 15, 18, 19, 21, 26], the homotopy analysis method [11, 27, 28] and the equivalent method [14, 18, 20, 29, 30]. These methods have succeeded in 1D models, and predict their typical amplitude-dependent properties. However, the increase in dimensionality from 1 to 2D NAM models introduces a significant number of nonlinear eigenvalue equations, leading to challenges in finding solutions of nonlinear eigenfrequencies and eigenvectors for describing the 2D nonlinear band structure.

While most analyses are confined to 1D models, there is a notable lack of research on 2D or higher dimensional models. Although the studies have uncovered several mechanisms governing wave suppression in finite NAM plates [9, 12], detailed analysis and explanations of the amplitude-dependent bandgap properties were not provided. Furthermore, as demonstrated in our recent studies on 1D NAM models [18, 19], nonlinear bands do not merely exhibit a shift as frequency changes. Instead, NAM bandgaps are adaptive to propagation distance and time, thus displaying band degeneration with bifurcation, evidenced by dispersion curve shortening, merging or even disappearance [27, 31, 32]. Band degeneration depends on the configuration of the coupled nonlinear metacells [19]. Different from 1D models, spatial divergence occurs in 2D structures that needs to be incorporated into 2D models. The associated effects on self-adaptivity and band degeneration remain unclear. It goes with saying that the self-adaptivity, band degeneration, along with the general amplitude dependency will all shape the wave propagation process. Moreover, although the vibration reduction of finite 2D NAM normal or sandwich plates has been extensively studied, and nonreciprocal wave manipulation has been realized in 1D elastic or acoustic diodes [33–37], the nonreciprocal phenomena in 2D space have rarely been studied.

Based on the above analysis, we introduce and model an infinite meta-plate model embedded with strongly nonlinear resonators in this paper, propose analytical methods to predict the band structure and wave attenuation, and validate these results numerically. We further scrutinize the phenomenon of "band degeneration" and its underlying physical mechanisms in a 2D plate. In particular, we elucidate the influence of the spatial divergence on the self-adaptivity and band degeneration. Based on the band properties, the linear and nonlinear meta-plates for breaking the reciprocal wave propagation are explored.

2 Nonlinear metamaterial plate and analysis methods

2.1 Finite element model of the NAM plate

As shown in Fig. 1, we examine an infinite meta-plate consisting of a substrate plate and periodical nonlinear resonators attached on the plate. The substrate plate is made of aluminum alloy. Its thickness h, density ρ, elastic modulus E, and Poisson's ratio v are 0.004 m, 2700 kg/m^3, 67 GPa and 0.3, respectively. A metacell is square, with a lattice constant $a = 0.04$ m. The concentrated mass m_0 embedded in the plate couples to the 2DoF nonlinear resonators with m_1, m_2 and linear stiffness k_1, k_2, as shown in Fig. 1b. Damping is not considered. The displacements of m_0, m_1 and m_2 are w_0, w_1 and w_2, respectively. Geometrical nonlinearity in the plate is not considered; therefore, nonlinearity arises solely from the resonators, with k_{2N} denoting the nonlinear stiffness coefficients. Parameters are: $m_0 = 0.06$ kg, $m_1 = 0.05$ kg, $m_2 = 0.05$ kg; $k_1 = 2.842 \times 10^4$ N/m, $k_2 = 1.263 \times 10^4$ N/m, $k_3 = 7.165 \times 10^4$ N/m. We take $k_{2N} = 1 \times 10^{13}$ N/m^3 to show the nonlinear phenomena. Thus, the equations of motion for the i^{th} resonator writes:

$$\begin{cases} m_0\ddot{w}_{0i} = k_1(w_{1i} - w_{0i}) + k_3(w_{2i} - w_{0i}) \\ m_1\ddot{w}_{1i} = -k_1(w_{1i} - w_{0i}) + k_2(w_{2i} - w_{1i}) + k_{2N}(w_{2i} - w_{1i})^n \quad (n = 3, 5, 7...) \\ m_2\ddot{w}_{2i} = -k_2(w_{2i} - w_{1i}) - k_{2N}(w_{2i} - w_{1i})^n - k_3(w_{2i} - w_{0i}) \end{cases} \tag{1}$$

The mathematical expressions are general and inclusive, covering a nonlinear factor n that may be achieved through oscillating unit design. For example, the system becomes a Duffing system when $n = 3$; whilst a large n can approximate a vibro-impact oscillator [38]. Here, we adopt the cubic stiffness

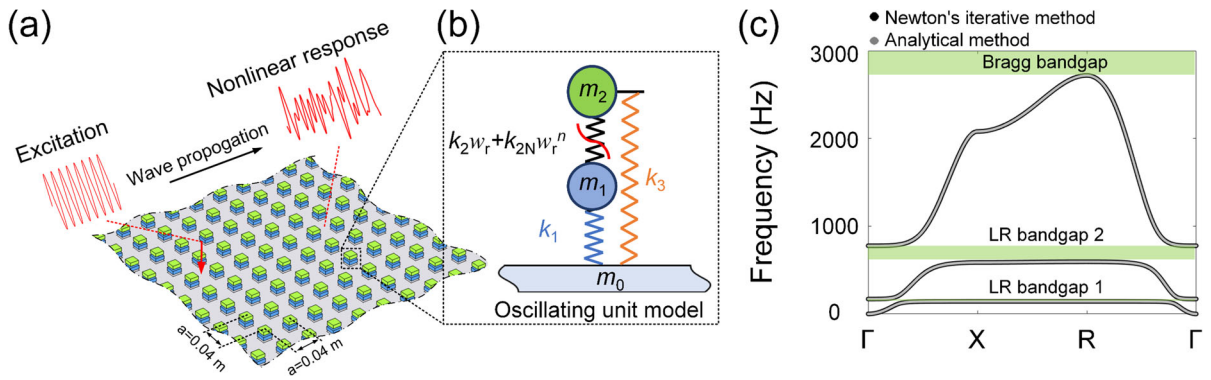

Fig. 1 Metamaterial model. **a** Schematic of an infinite plate with periodically arranged nonlinear oscillators. **b** Equivalent model of the nonlinear oscillators. **c** Dispersion curves of the linear metamaterial plate by analytical methods ($k_{2N} = 0$). The green areas are local resonant and Bragg bandgaps

nonlinearity ($n = 3$), as used in many studies [18, 19], to show the salient phenomena in the system. This means, the nonlinear force between m_1 and m_2 is $F_N(t)_i = k_2 w_{ri} + k_{2N} {w_{ri}}^3$.

Denoting the relative displacement $w_{ri} = w_{2i} - w_{1i}$, Eq. (1) can be simplified as:

$$\mathbf{M}_c \ddot{\mathbf{w}}_{ci} + \mathbf{K}_c \mathbf{w}_{ci} + \mathbf{K}_{Nc} \mathbf{w}_{ci}^3 = \mathbf{0} \tag{2}$$

where $\mathbf{M}_c = \begin{bmatrix} m_0 & 0 & 0 \\ 0 & m_1 & 0 \\ 0 & m_2 & m_2 \end{bmatrix}$, $\mathbf{K}_c = \begin{bmatrix} k_1+k_3 & -k_1-k_3 & -k_3 \\ -k_1 & k_1 & -k_2 \\ -k_3 & k_3 & k_2+k_3 \end{bmatrix}$, $\mathbf{K}_{Nc} = \begin{bmatrix} 0 & 0 & 0 \\ 0 & 0 & -k_{2N} \\ 0 & 0 & k_{2N} \end{bmatrix}$ and $\mathbf{w}_{ci} = \begin{bmatrix} w_0 \\ w_1 \\ w_r \end{bmatrix}_i$.

Then, we establish the meta-plate model with the finite element method under the Kirchhoff–Love plate theory [12] (see Appendix A.1). The equations of motion for the i^{th} metacell writes:

$$\mathbf{M}\ddot{\mathbf{w}}_i + \mathbf{K}\mathbf{w}_i + \mathbf{K}_N \mathbf{w}_i^3 = \mathbf{0} \tag{3}$$

To solve Eq. (3), we adopt the first-order harmonic balance method by assuming the solution as:

$$\mathbf{w}_i = \mathbf{q}_i \sin(\Omega t) \tag{4}$$

where $\mathbf{q}_i$ stands for the amplitudes of $\mathbf{w}_i$, and $\Omega = 2\pi f$. Substituting Eq. (4) into (3) and balancing the coefficients of $\sin(\Omega t)$ gives:

$$(\mathbf{K} - \Omega^2 \mathbf{M})\mathbf{q}_i + \frac{3}{4}\mathbf{K}_N \mathbf{q}_i^3 = \mathbf{0} \tag{5}$$

According to the Ref. [19], Bloch-Floquet theorem can be used to deal with nonlinear systems despite some limitations. Here, we will also use it to solve the above system to obtain the dispersion curves and then illustrate its limitations. According to Bloch-Floquet theorem (see Appendix A.2), Eq. (5) can be rewritten as:

$$(\tilde{\mathbf{K}} - \Omega^2 \tilde{\mathbf{M}})\tilde{\mathbf{q}}_i + \frac{3}{4}\tilde{\mathbf{K}}_N \tilde{\mathbf{q}}_i^3 = \mathbf{0} \tag{6}$$

Note that Bloch-Floquet theorem is rigorously established for linear periodic structures [39]. For nonlinear ones, the use of this theorem should be regarded as an approximate method to substitute the periodic boundary conditions [40].

2.2 Shooting-Newton iteration method for calculating the band structure

To solve the dispersion curves of the 2D model, we must find the eigenfrequency Ω and the eigenvector $\tilde{\mathbf{q}}_i$ of Eq. (6) by specifying the input displacement A_0 on mass m_0 and assigning wave numbers κ_x and $\kappa_y \in [0, \pi]$. The Newton iteration is obtained to find the roots of the eigenfrequency Ω and the corresponding eigenvector $\tilde{\mathbf{q}}_i$ by specifying proper initial guesses of the solutions. As the initial guess determines the convergency and the results, sweeping the initial guesses in proper parameter space by Shooting method [41–43] can find all dispersion curves and relevant wave modes.

The initial vector $\tilde{\mathbf{q}}_{0i}$ is set to $\mathbf{0}$ for a given initial frequency $\Omega_0 \in [0, 3000]$ Hz. When all frequencies $\Omega_0 \in [0, 3000]$ Hz are shot in sequence through Newton's iterations, all solutions of $\tilde{\mathbf{q}}_i$ and eigenfrequencies Ω are captured, as it is called the "Shooting method". The normalized eigenvector $\tilde{\mathbf{q}}_i/A_0$ represents the corresponding wave mode.

To verify the method, we calculate the dispersion curves for the corresponding linear metamaterial model (with $k_{2N} = 0$) in the range of [0, 3000] Hz. In the linear model, the eigenfrequency Ω and the eigenvector $\tilde{\mathbf{q}}_i$ are obtained directly, allowing us to compare these results with those obtained via the Shooting method. As shown in Fig. 1c, the results correlate well with each other. For nonlinear models, solutions from the Shooting-Newton iteration method all are convergent (see Appendix A.3).

2.3 Methods for predicting wave attenuation

The above method is employed to ascertain the eigenfrequency associated with a specific wave number κ_x and κ_y. Conversely, the real part κ_R and the imaginary part κ_I of the wave numbers ($\kappa = \kappa_R + i\kappa_I$) can be predicted for a given frequency. Under the input from a point, the wave in a generic 2D meta-plate evolves as a function of time, t, and propagation distance, r:

$$u(r,t) = A(r)e^{i(\kappa_R r - \Omega t)}, \qquad A(r) = A_0 g_{\text{space}}(r) g_{\text{bandgap}}(r) \tag{7}$$

where A_0 is the source amplitude. The attenuation coefficient induced by bandgap g_{bandgap} can be calculated as:

$$g_{\text{bandgap}}(r) = e^{-\kappa_I r} \tag{8}$$

In theory, the amplitude of a point source would generate a cylindrical wave that would also fluctuate (far field) as an exponential law [44]:

$$g_{\text{cylindrical}}(r) = \sqrt{\frac{2}{\pi\gamma r}} e^{i(\gamma r - \frac{1}{4}\pi)} \tag{9}$$

where γ denotes the wave number of the plate $\gamma = \sqrt{\Omega}(\frac{\rho h}{D})^{1/4}$ and $D = \frac{Eh^3}{12(1-\nu^2)}$ represents the flexural stiffness. This means the amplitude of a point source would decay as $r^{-0.5}$.

This model allows for distinguishing the attenuation induced by the bandgap and that by the spatial divergence of the wave. κ_I, as an important parameter, cannot be directly determined by using the method for calculating the band structure, as it will yield a multitude of solutions whose physical meanings can hardly be established. Instead, we use the equivalent linearized approach based on the bifurcation to solve the equivalent stiffness between m_1 and m_2 for nonlinear models (see Appendix A.4), which has been experimentally demonstrated in Ref. [18].

3 Properties of 2D nonlinear band structure and wave propagation

3.1 Typical 2D band structure of the nonlinear meta-plate

Before discussing the evolution process, we present the result of a typical case with $A_0 = 10$ μm to illustrate the salient properties of this nonlinear system. The bands are calculated using the Shooting-Newton iteration method, which requires a substantial amount of time to find a convergent solution for a given set of parameters.

The specified model parameters, the linear counterpart of the meta-plate generates a Bragg bandgap (from 2718 Hz on) and two locally resonant bandgaps: denoted as LR1 (143.2, 170.2) Hz and LR2 (595.6, 777.9) Hz bandgaps.

For specified wave vectors κ_x and κ_y in Eq. (6), the frequency solution is $f = \Omega/2\pi = f_R + if_I$, where f_R and f_I denote the real and imaginary parts, respectively, as shown in Fig. 2a, b. Solutions with a nonzero imaginary part (red curve) imply wave attenuation [19] and are therefore excluded from the band structure. The final processed band structure is presented in Fig. 2c. Unlike 1D structures, 2D structures feature additional Bloch vectors, **X** and **R,** in the band structure. The first frequencies at points **X** and **R** shift upwards to 329.0 and 353.5 Hz, respectively; while the second frequencies at points **X** and **R** shift upward to 743.0 and 1152.5 Hz, respectively, with the third curve remaining intact. The shift leads to the disappearance of the LR1 and LR2 bandgaps.

Moreover, the nonlinearity significantly affects the dispersion properties of the 2D meta-plate, which can be observed in the group velocity, $c_g = d\Omega/dk$, shown in Fig. 2d. It is observed that certain group velocity curves exhibit asymmetry, which is attributed to the asymmetry in the slope of the dispersion curve shown in Fig. 2c. The group velocity shows variations in the number of rings: the first curve changes from a single ring (orange) to a double ring (blue), the second curve

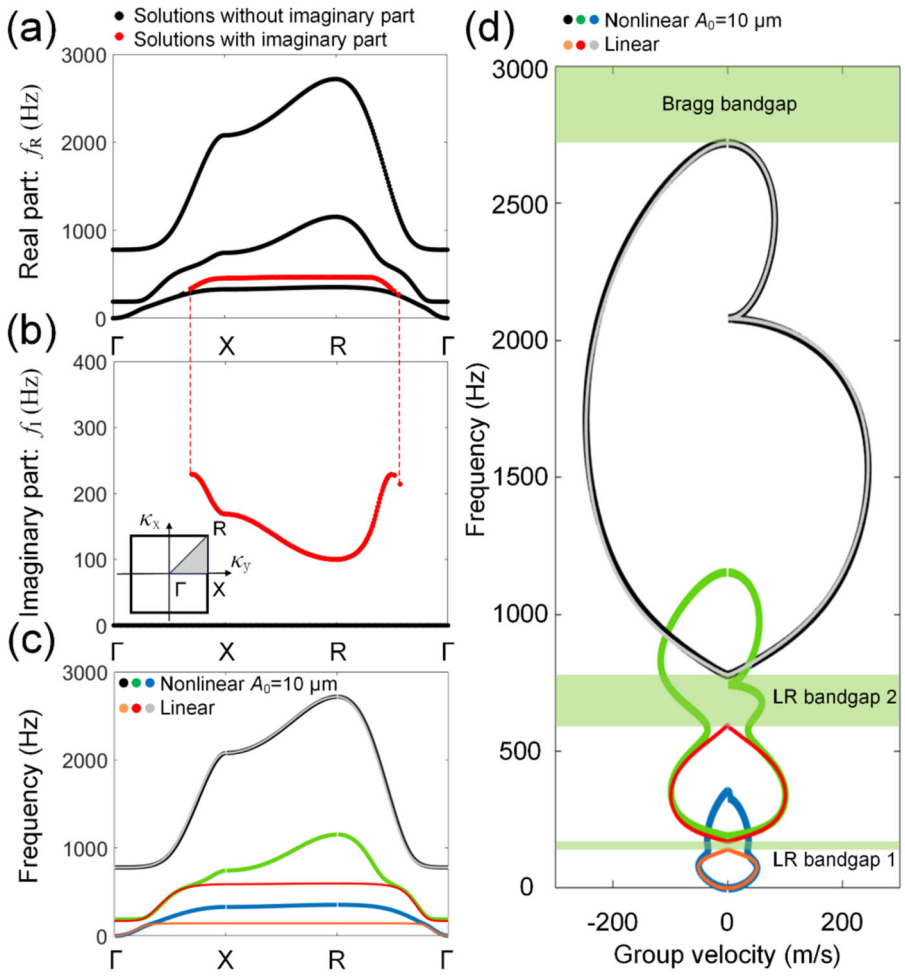

Fig. 2 Dispersion curves of nonlinear meta-plate with A_0 = 10 μm. **a** and **b** Real part f_R (black line) and imaginary part f_I (red line) of the curves, respectively. **c** Curves only with real numbers (i.e., f_I = 0), compared to that of the linear model. **d** Variation of group velocities between linear and nonlinear models. The colors correspond to those of (**c**)

changes from a single ring (red) to a triple ring (green), while the third curve remains unchanged with a double ring (grey and black). Owing to these variations, the group velocities become non-zero within the previously existing LR1 and LR2 bandgaps, spanning from (0, 143.2) Hz to (0, 353.5) Hz and from (170.2, 595.6) Hz to (188.5, 1152.5) Hz, respectively. This is evidenced by the disappearance of the LR1 and LR2 bandgaps with respect to the group velocity.

3.2 Evolution of 2D band structure

Besides the changes in bandgap range and group velocity, the strong nonlinearity also alters the wave modes along the band structure, evident through a degeneration process [19]. To show the evolution process of the 2D band structure, the nonlinear band structures and wave modes with increasing A_0 are studied in the following analyses. We take five typical cases to illustrate its variation process, as shown in Fig. 3.

When the nonlinearity is very weak (A_0 = 1 μm), there are three dispersion curves, as in the linear model. As A_0 increases, the first curve arches upwards from the center, spanning from (0, 143.6) to (0, 418.9) Hz; the second curve also arches upwards from the center and simultaneously shifts upwards overall. Eventually, it merges with the third curve, covering from (170.2, 595.6) Hz to (788.9, 2718) Hz; the third curve remains nearly unchanged initially but starts to

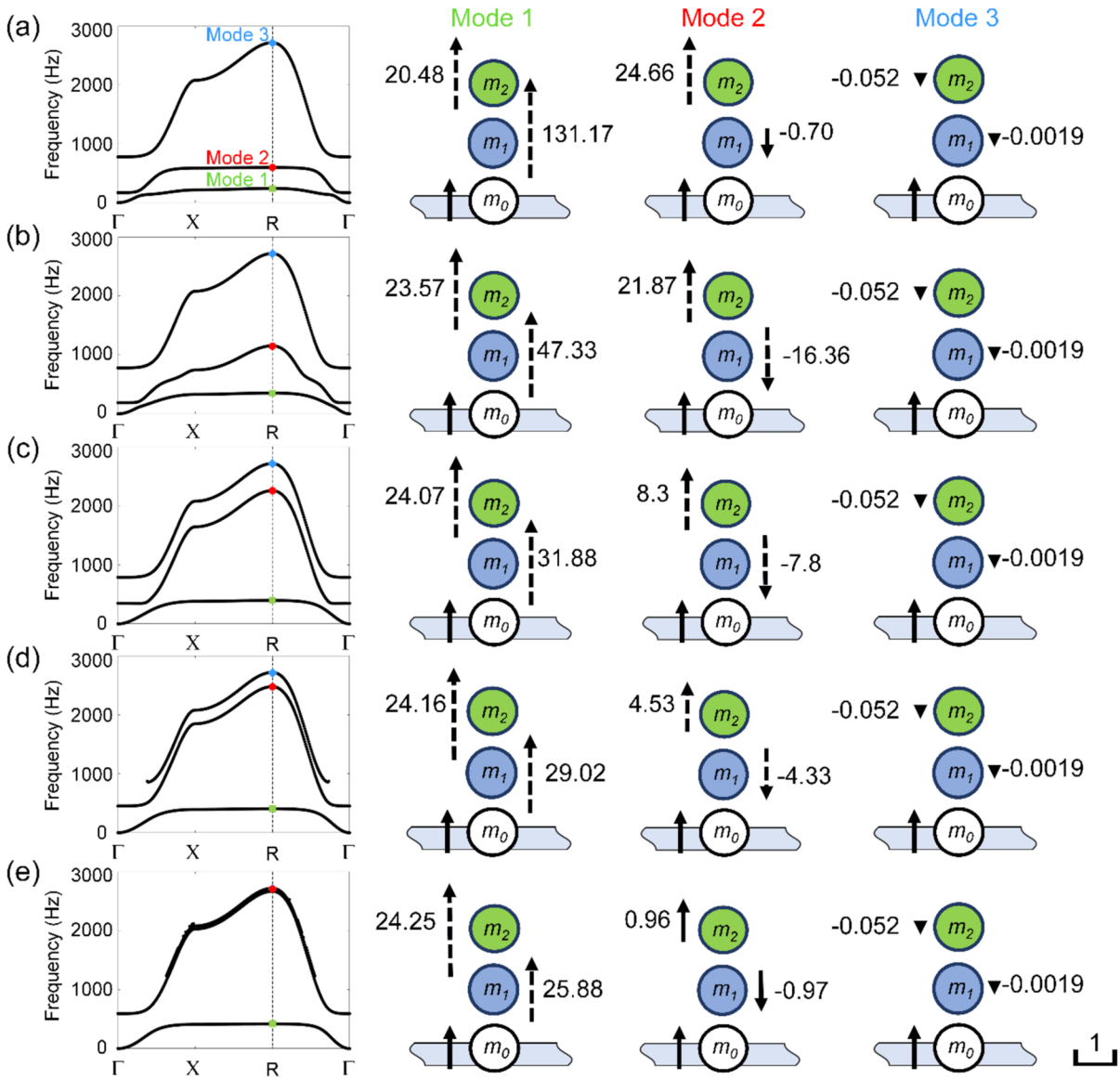

Fig. 3 Evolutions of dispersion curves and wave modes with increasing incident amplitude A_0. **a–e** five typical cases showing their dispersion curves and wave modes: **a** Case-1: very weak nonlinearity (A_0 = 1 μm). **b** Case-2: weak nonlinearity (A_0 = 10 μm). **c** Case-3: moderate nonlinearity (A_0 = 50 μm). **d** Case-4: strong nonlinearity (A_0 = 100 μm). **e** Case-5: stronger nonlinearity (A_0 = 500 μm). Modes 1 2 and 3 show the wave modes of the resonator at Bloch wave vector **R** in dispersion curves, respectively. The length and the direction of arrows denote the generalized length A_v/A_0 and the corresponding phase (positive or negative), respectively. Numbers (value = A_v/A_0, v = 0, 1, 2) are labelled near arrows. The arrow length of m_0 is set to 1, and other arrows are presented relative to 1. Some arrows are dashed lines as the value A_v/A_0 is so large, which are truncated in length and presented by dashed arrows

degenerate and shorten as the nonlinearity increases, as shown in Fig. 3d. Ultimately, the third curve merges with the second curve, as shown in Fig. 3e. Overall, the three dispersion curves degenerate into two, and the two resonant bandgaps merge into one with a higher and broader range.

Importantly, for the 2D band, the variation in the bandgaps can be manifested by examining the solution at point **R** of the reciprocal lattice. We can further investigate the wave modes at point **R** for a deeper understanding of the phenomena.

The shift of the first and second curves leads to the modulation of the LR1 bandgap: it resembles that of the linear model when the input level is weak, $A_0 << 1$ μm, but becomes blind at $A_0 \approx 1$ μm, and then reopens when $A_0 > 70$ μm. Wave mode 1 sheds light on the mechanism. By increasing A_0 from 1 to 500 μm, A_1/A_2 decreases from 6.4 to 1.07, suggesting a transition from the "local resonance of m_1" mode to "synchronous local resonance of m_1 and m_2" mode, i.e. the LR1 bandgap transforms into a new nonlinear locally resonant (NLR) bandgap.

The degeneration of the LR2 bandgap is primarily due to the merging of the second and third curves: it becomes blind at $A_0 \approx 7$ μm and eventually disappears. The variation of wave modes 2 and 3 also confirms this. As shown in mode 2 of Fig. 3a–e, when A_0 increases from zero to 500 μm, the phases of m_1 and m_2 remain opposite, $|A_1/A_0|$ increases until the LR2 bandgap becomes blind, $|A_1/A_0|$ decreases to 0.97, and $|A_2/A_0|$ decreases from 24.66 to 0.96. Throughout this process, mode 3 remains invariant. When the nonlinearity becomes sufficiently strong, $|A_1/A_0|$ and $|A_2/A_0|$ both approach zero, and the positive or negative sign has negligible influence on the wave dynamics. Modes 2 and 3 merge, both exhibiting Bragg scattering. Hence, the LR2 bandgap shifts from the "local resonance of m_2" to "scattering between m_0", i.e. the LR2 bandgap merges into a Bragg bandgap.

Overall, the merging of modes 2 and 3 causes the three bandgaps (LR1, LR2 bandgaps and a Bragg bandgap) to retreat and degenerate into two bandgaps (NLR bandgap and a Bragg bandgap) with enhanced nonlinearity. This transformation of the nonlinear meta-plate turns a 3DoF unit into a 2DoF unit under strong nonlinearity.

The dimensionality reduction and enhanced nonlinearity observed are similar to those reported in Ref. [19], suggesting that the band degeneration and evolution also apply to high-dimensional nonlinear metamaterials. Thus, we will not consider the other situations where nonlinearity appears between m_1-m_2, m_0-m_2, or m_0-m_0.

3.3 Wave attenuation in the nonlinear meta-plate

To demonstrate these degeneration processes, we numerically examine the wave propagation in an infinite meta-plate with numerical integration method. As shown in Fig. 4a, the model consists of a meta-plate in the center surrounded by a plate frame with large damping to minimize wave reflection. The central meta-plate consists of 30 × 30 units. The surrounding large damping plates can almost completely attenuate the incident wave, thus creating a non-reflecting boundary for time-domain simulations. An excitation is applied at the center point of the model. We define the transmission rate T from the time domain as:

$$T = 20\log_{10}(A_{0\_\text{output}}/A_0)\ (\text{dB}) \tag{10}$$

where A_{0_output} is the peak value of the output wave amplitude. A standard 10-cycle sinusoidal signal with 2-cycle smooth tails is used as the input wave, launched at the center point shown in Fig. 4c. The output wave packet exhibits minimal reflections in Fig. 4d, confirming the effectiveness of the non-reflective boundary design. Figure 4b shows that the transmissions in the X-direction of the plate are found to be consistent when calculated numerically and theoretically. This confirms the accuracy of the theoretical prediction of the spatial divergence by Eq. (9).

As shown in Fig. 5a–c, with increasing A_0, the colored "bandgap" area transitions from the LR2 bandgap (595.6–777.9 Hz) to the NLR bandgap (418.9–592.4 Hz). Consequently, we numerically calculate the transmission T in the range of (400, 800) Hz with increasing A_0 to validate the existence of LR2 and NLR bandgaps as shown in Fig. 5d–i. In Fig. 4b, it is observed that the cylindrical wave, subjected to the spatial divergence, undergoes a transmission loss of approximately − 12 dB at the 8th unit. Thus, any transmission significantly lower than − 12 dB indicates attenuation by the bandgap. The linear bandgap in the range of (595.6, 777.9) Hz results in a reduction of more than 26 dB, as shown in Fig. 5d, g.

When the nonlinearity becomes strong (A_0 = 100 μm) as shown in Fig. 5e, h, the 8th transmission in the range of (409, 453) Hz is only − 15 dB, indicating a weak "bandgap" effect. Although both the spatial divergence and the bandgap effect serve to attenuate wave, the former maybe stronger than the latter for waves in the bandgap range, which is demonstrated in Sect. 3.4.

When nonlinearity further intensifies (A_0 = 500 μm) as shown in Fig. 5f, i, the 8th transmissions in the range of (418.9, 592.4) Hz are all below − 17 dB (significantly smaller than − 12 dB) in both 0 and 45 degrees from X-direction, indicating a strong

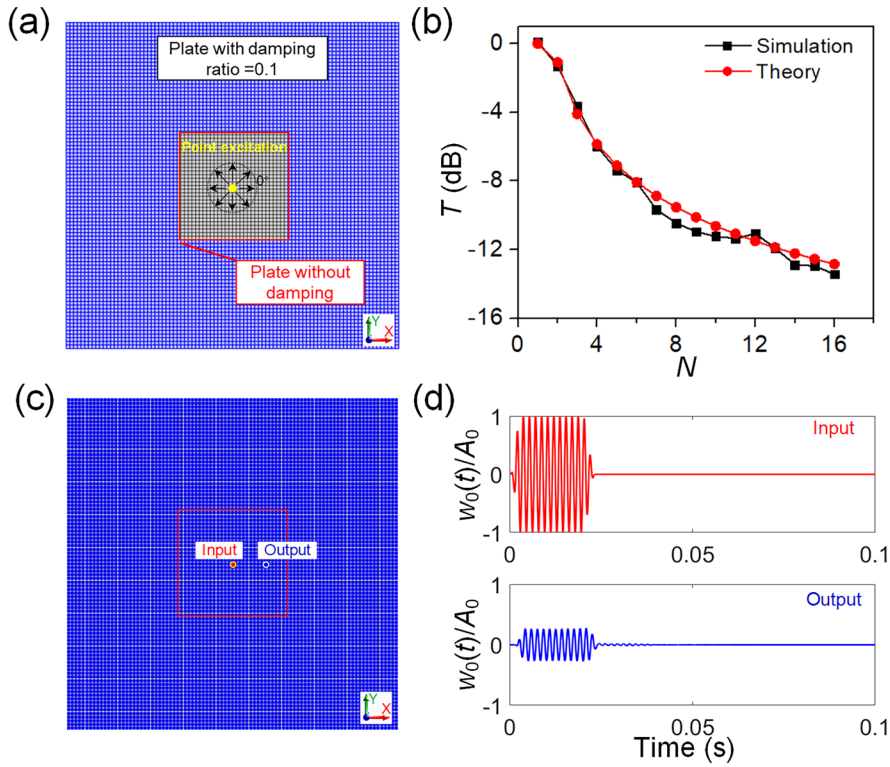

Fig. 4 Setup of simulation for modelling the meta-plate. **a** Damping setup for modelling an infinite plate. The wave from the point excitation can be absorbed by the plate with damping (blue area) to create a non-reflecting boundary for the plate within red square. **b** Transmission in the *X*-direction started from the point excitation. **c** The layout of resonator. One blue point represents a resonator. **d** Normalized time domains of input and output samples in **c** at 400 Hz

"bandgap" effect. In such case, the bandgap effect becomes stronger than the spatial divergence and plays a dominant role in the total attenuation, which is also demonstrated in detail in Sect. 3.4.

3.4 Contributions of wave attenuation from bandgap effect and spatial divergence

We examine some typical wave propagation under different initial amplitudes to clarify the contributions of the attenuation induced by the bandgap effect and that by the spatial divergence, as shown in Fig. 6. 440 Hz is chosen from the Fig. 5e, f, for A_0 = 100 μm and A_0 = 500 μm, in the predicted bandgap (green and red areas).

When the response amplitude of the n^{th} metacell A_n (n = 0, 1, … 13) from the source n = 0 is given, the imaginary part κ_{I}, denoting the attenuation from the bandgap, can be obtained using the equivalent linearized approach (see Appendix A.4). From n^{th} to $(n+1)^{\text{th}}$ metacell, the wave propagation distance is the lattice constant a, and the attenuation induced by bandgap g_{gap} is given by Eq. (8):

$$g_{\text{gap}} = g_{\text{bandgap}}(a) = e^{-\kappa_{\text{I}} a}. \tag{11}$$

The attenuation induced by spatial divergence g_{space} is given by Eq. (9):

$$\begin{cases} g_{space} = g_{\text{cylindrical}}(a) = \sqrt{\dfrac{2}{\pi\gamma a}} e^{i(\gamma a - \frac{1}{4}\pi)} \quad (n=0) \\ g_{space} = g_{\text{cylindrical}}((n+1)a)/g_{\text{cylindrical}}(na) = \sqrt{\dfrac{n}{(n+1)}} e^{i\gamma a} \\ \qquad\qquad (n=1,2,\ldots,14) \end{cases} \tag{12}$$

Thus, the total response amplitude $A_{n+1} = A_n g_{space} g_{gap}$ can be obtained by Eq. (7). Since the input amplitude undergoes a change from A_n to A_{n+1}, the nonlinear band degenerates self-adaptively due to the amplitude-dependent properties. Therefore, A_{n+1} is taken as the input amplitude to calculate A_{n+2}. Repeating the above steps, the specific attenuations for each unit can be calculated as shown in Fig. 6 (solid line). Numerically, all g_{space} and A_{n+1} (n = 0, 1, … 13) can be obtained in the numerical calculations as shown in Figs. 4b and 5e–f, respectively. Since $A_{n+1} = A_n g_{space} g_{gap}$, the numerical g_{gap} can be separated, as shown in Fig. 6 (dash line).

When A_0 = 100 μm (Fig. 6a), the wave amplitude at the first metacell is $A_1 \approx$ 54.9 μm, i.e., the total

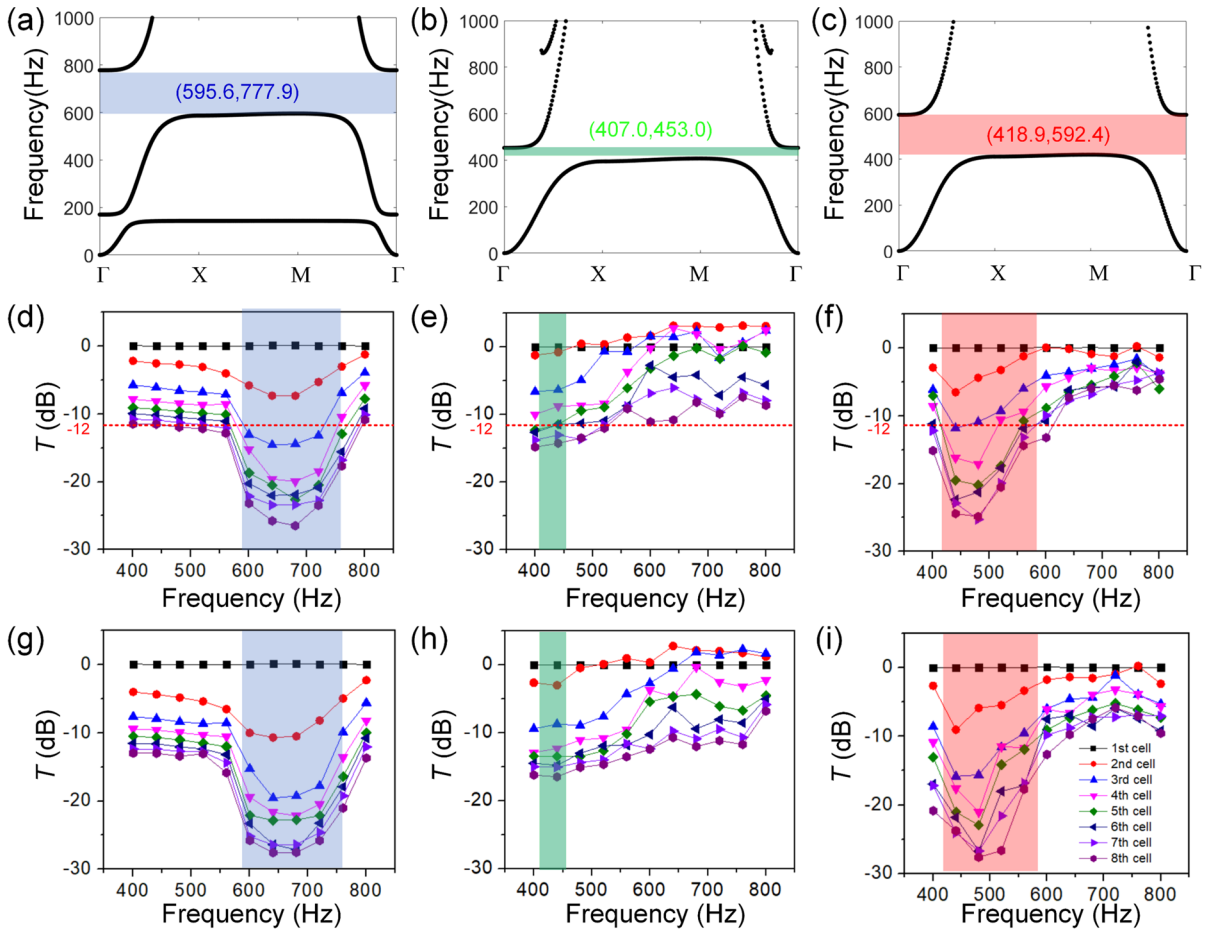

Fig. 5 Numerical validation of Linear and nonlinear band structure. **a**–**c** Dispersion curves by the Shooting-Newton iteration method. **d**–**f** Transmissions in the *X*-direction of the meta-plate. **g**–**i** Transmissions at 45 degrees from the *X*-direction of the meta-plate. **a**, **d**, **g** Case-1: Linear band structure. **b**, **e**, **h** Case-2: strong nonlinearity (A_0 = 100 μm). **c**, **f**, **i** Case-3: stronger nonlinearity (A_0 = 500 μm). Different colored areas show the bandgap calculated by the Shooting-Newton iteration method

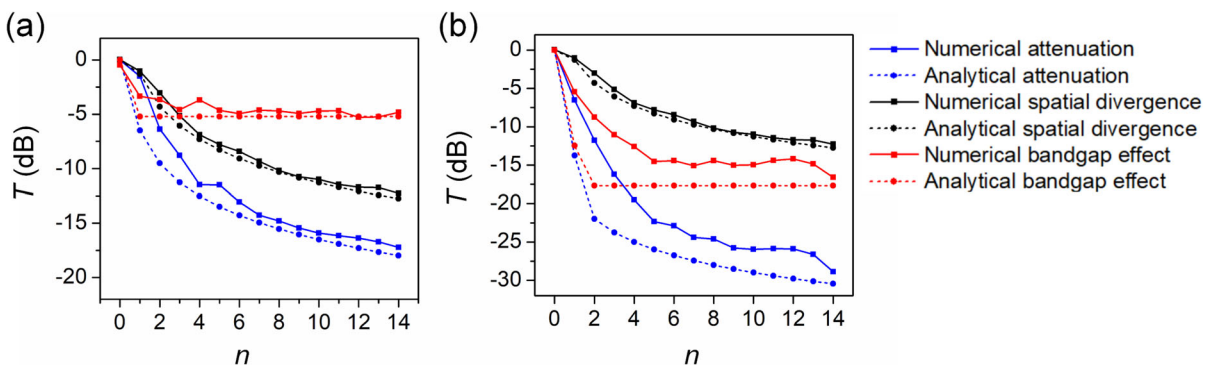

Fig. 6 Specific attenuation induced by the spatial divergence (black), the bandgap effect (red) and the total (blue). **a** A_0 = 100 μm; **b** A_0 = 500 μm

attenuation is − 6.5 dB. The attenuation induced by the bandgap effect and the spatial divergence are calculated as − 5.21 and − 1.29 dB, respectively. However, for $n \geq 2$, the bandgap is shift downward, and the wave frequency 440 Hz is outside the bandgap. In this case, the spatial divergence dominates the subsequent attenuation, thus featuring a amplitude attenuation trend similar to that of the spatial divergence.

When A_0 = 500 μm (Fig. 6b), $A_1 \approx$ 100 μm and $A_2 \approx$ 39.8 μm. As predicted analytically, the significant attenuation in the two metacells, − 17.68 dB, is induced by the nonlinear bandgap, although its frequency range changes during wave propagation. Here, the spatial divergence induces attenuation by − 4.3 dB, much lower than that by the bandgap effect. However, for $n \geq 3$, as the amplitude is so low that the wave at 440 Hz jumps out of the bandgap again. As a result, the spatial divergence dominates the wave attenuation.

Overall, it can be concluded that the nonlinear bandgap exerts "local" attenuation effect. For frequencies in the bandgap for specific amplitude A_0, like 440 Hz for A_0 = 100 or 500 μm, the bandgap only shows its effects near the excitation point. The bandgap is preserved in a longer propagation distance for higher incident amplitude. Although its effect is local, the induced attenuation is significant. When the wave frequency jumps out of a self-adaptive bandgap, or disappears in the bandgap, the attenuation is dominated by the spatial divergence. This also suggests that the nonlinear bandgap varies self-adaptively as the propagation distance/time increases as reported in Ref. [19], but the introduction of the spatial divergence accelerates this process in a 2D NAM.

4 2D nonreciprocity properties enabled by nonlinear meta-plate

As well known, leveraging proper nonlinear interactions can enable nonreciprocal wave transmission. As demonstrated, nonreciprocal propagation can be induced by high- or sub-harmonics [45–48], bifurcations and chaos [46, 48], and amplitude-dependent bandgaps [49, 50]. More specifically, a sub-wavelength, bidirectional elastic diode with frequency-preserved nonreciprocity was experimentally demonstrated by coupling nonlinear and linear chains [33]. In linear systems, the directional nature of wave propagation in a 2D monatomic lattice is taken advantage to break reciprocity [51]. However, studies on nonlinear nonreciprocity are currently limited to 1D systems. Extension to 2D systems presents challenges due to the aforementioned challenges in numerical calculations and analyses and structural complexities. Our NAM plate offers the opportunity to examine this important issue. Nonreciprocal wave propagation can be realized by integrating the linear and nonlinear meta-plate together.

Furthermore, the investigation into the evolution of the band structure with increasing nonlinearity suggests that the nonlinear bandgap can be manipulated through regulating the wave amplitude. Conversely, the linear bandgap remains unaltered in response to a change in wave amplitude. Therefore, nonreciprocal wave propagation can be realized by integrating the linear and nonlinear meta-plates together.

4.1 Model and methods

As shown in Fig. 7a, we introduce 5 × 90 linear resonators (represented by green points) and 5 × 90 nonlinear oscillating units (represented by orange points) in the middle part of the plate. Figure 7b shows an enlarged view of the asymmetrical region of the combined plate.

Points A and B serve as the wave origin points for the left and right plates, respectively. The propagation from A_m to B_n is labelled as "A_m2B_n" or "Lin2Non" subsequently. In linear systems (with $k_{2N} = 0$), A2B = B2A in both the time and frequency domains, indicating reciprocity. For nonlinear systems, A2B ≠ B2A in both domains, signifying nonreciprocity as illustrated in Fig. 7e, f. The mechanisms underlying this phenomenon will be elucidated subsequently. To quantify wave propagation, we take a typical case of A2B to define the transmissions in the time and frequency domains as:

$$T_{\text{time\_A2B}} = 20\log_{10}[\mathrm{A}_{0\_\text{A2B}}^{(\text{Time})}/\mathrm{A}_0]\ (\text{dB}), \tag{13}$$

$$T_{\text{Freq\_A2B}} = 20\log_{10}[\mathrm{A}_{0\_\text{A2B}}^{(\text{Freq})}/\mathrm{A}_0]\ (\text{dB}), \tag{14}$$

where $A_{0\_\text{A2B}}^{(\text{Time})}$ denotes the average time-domain output amplitude when the input is A_0; $A_{0\_\text{A2B}}^{(\text{Freq})}$ is picked from the frequency spectra at the incident frequency, as

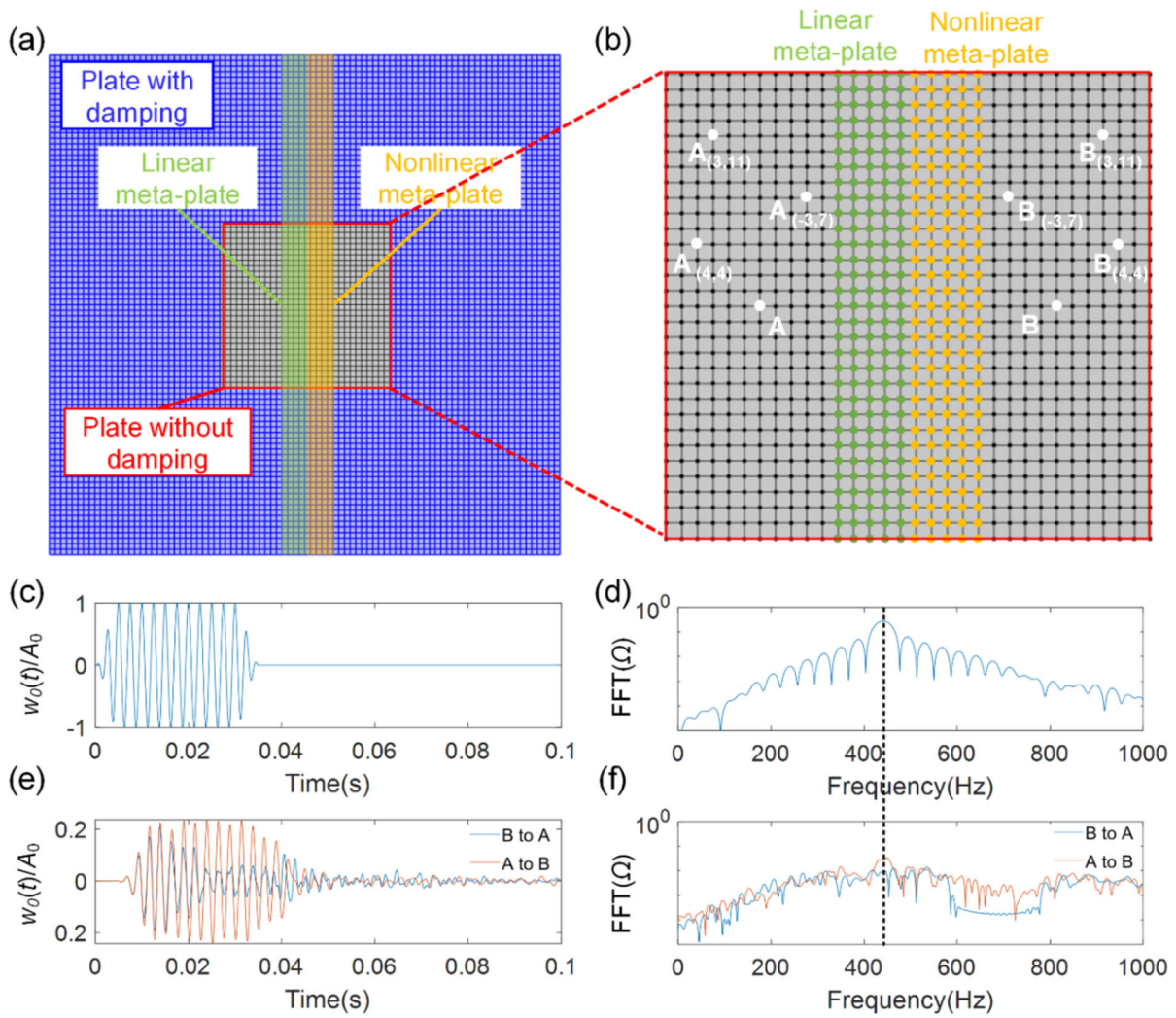

Fig. 7 Elastic diode in the meta-plate. **a** Schematic diagram of our bidirectional diode plate consisting the linear meta-plate (green area) and nonlinear meta-plate (orange area). Except for the nonlinear and linear meta-plate, the other setup is same as that in Fig. 4a. **b** Enlargement of undamped region within the red square in (**a**). Each green point represents one linear oscillating unit, each orange point represents one nonlinear oscillating unit, and each black point represents the plate. **c** Normalized time domain of an input sample at 440 Hz. **d** Frequency spectra of (**c**). **e** Normalized time domains of outputs "A2B". "A2B" refers to the output of B when it is excited by the input of A in (**b**). **f** Frequency spectra of (**e**)

shown in Fig. 7d, f. As there are multiple harmonics, $T_{\text{Time\_A2B}}$ represents the transmission containing all frequency components; $T_{\text{Freq\_A2B}}$ represents the transmission of the fundamental wave only.

To differentiate the degrees of such point-to-point reciprocity, we define:

$$\Delta T_{\text{Time\_A2B}} = T_{\text{Time\_A2B}} - T_{\text{Time\_B2A}} \text{ (dB)} \tag{15}$$

$$\Delta T_{\text{Freq\_A2B}} = T_{\text{Freq\_A2B}} - T_{\text{Freq\_B2A}} \text{ (dB)} \tag{16}$$

In addition to the point-to-point nonreciprocity, we also quantify the reciprocity for the entire 2D plate using:

$$\Delta T_{\text{Time\_Lin2Non}} = \frac{\sum_{m=-5}^{6}\sum_{n=-15}^{15} T_{\text{Time\_A2B}(m,n)} - \sum_{m=-5}^{6}\sum_{n=-15}^{15} T_{\text{Time\_B2A}(m,n)}}{12 \times 31} \text{ (dB)} \tag{17}$$

$$\Delta T_{\text{Freq\_Lin2Non}} = \frac{\sum_{m=-5}^{6}\sum_{n=-15}^{15} T_{\text{Freq\_A2B}(m,n)} - \sum_{m=-5}^{6}\sum_{n=-15}^{15} T_{\text{Freq\_B2A}(m,n)}}{12\times 31} (\text{dB}) \quad (18)$$

Locations A and B mean the location (m, n) units from the wave emitting origins A and B, respectively, where $m \in$ [-5, 7] and $n \in$ [-15, 15], as labelled in Fig. 7b.

4.2 Typical features of nonreciprocity

Figure 8a–d show $T_{\text{Time\_A2B}}$, $T_{\text{Freq\_A2B}}$, $T_{\text{Time\_B2A}}$ and $T_{\text{Freq\_B2A}}$ within the range of (400, 800) Hz as A_0 increases, for A2B and B2A, respectively. Under weak nonlinearity at A_0 = 10 μm, $T_{\text{Time\_A2B}}$, $T_{\text{Freq\_A2B}}$ $T_{\text{Time\_B2A}}$, $T_{\text{Freq\_B2A}}$ are all low within the frequency range of (600, 760) Hz and high within (400, 560) Hz due to the LR2 bandgap in the range of (595.6, 777.9) Hz. As A_0 increases, for A2B depicted in Fig. 8a, b, only $T_{\text{Time\_A2B}}$ and $T_{\text{Freq\_A2B}}$ at (400, 480) Hz exhibit a slight decline, while remaining nearly constant at other frequencies. Conversely, for B2A shown in Fig. 8c, d, $T_{\text{Time\_A2B}}$ and $T_{\text{Freq\_A2B}}$ shift downwards noticeably at (400, 560) Hz and upward at (600, 760) Hz. Capitalizing on the different transmission patterns under weak and strong nonlinearity, nonreciprocal wave propagation between A and B can be achieved. As shown in Fig. 8e–l, we examine the specific situations of reciprocal wave propagation under four amplitudes, A_0 = 10, 100, 300, 500 μm.

For $A_0 < 300$ μm, the wave propagation between A and B is reciprocal, as the nonlinear resonant bandgap effects remain weak despite the presence of the nonlinearity. This occurs because the incident wave from points A or B diminishes due to the spatial wave divergence.

The wave amplitude becomes low when reaching the boundary of the meta-plate, thus inducing only weak nonlinearity. For $A_0 > 300$ μm, the wave propagation between A and B becomes nonreciprocal within the frequency ranges of (400, 440) and (600, 760) Hz. With A_0 further increasing to 500 μm, the

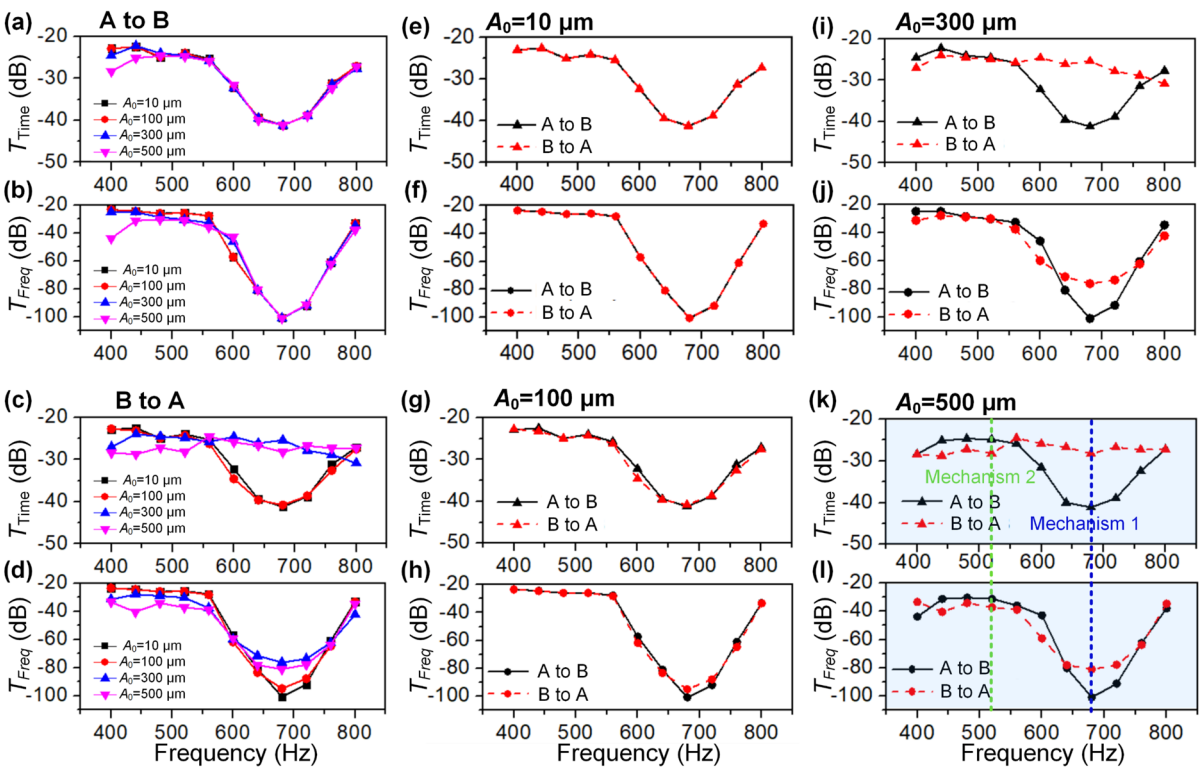

Fig. 8 $T_{\text{Time\_A2B}}$, $T_{\text{Time\_B2A}}$, $T_{\text{Freq\_A2B}}$ and $T_{\text{Freq\_B2A}}$ with increasing incident amplitude A_0. **a** $T_{\text{Time\_A2B}}$, **b** $T_{\text{Freq\_A2B}}$ **c** $T_{\text{Time\_B2A}}$, **d** $T_{\text{Freq\_B2A}}$ **e**, **f** Case-1: weak nonlinearity (A_0 = 10 μm). **g**, **h** Case-2: strong nonlinearity (A_0 = 100 μm). **i**, **j** Case-3: stronger nonlinearity (w_0 = 300 μm). **k**, **l** Case-4: stronger nonlinearity (A_0 = 500 μm)

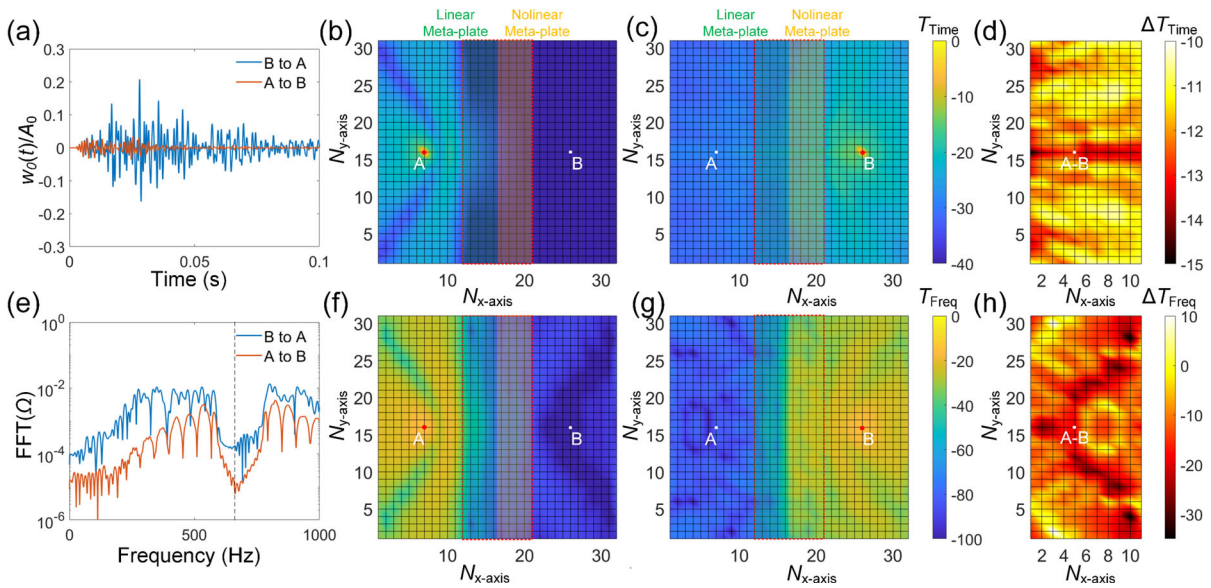

Fig. 9 Nonreciprocal wave propagation at input frequency 680 Hz in a plate with the integration of linear and nonlinear meta-plate. **a**, **e** Normalized time and frequency domains for B2A and A2B. **b**, **c** Distribution of $T_{\text{Time\_A2B}(m,\ n)}$ and $T_{\text{Time\_B2A}(m,\ n)}$ in the entire plate, respectively. **f**, **g** Distribution of $T_{\text{Freq\_A2B}(m,\ n)}$ and from $T_{\text{Freq\_B2A}(m,\ n)}$ in the entire plate, respectively. The red point indicates the point of excitation. **d**, **h** Distribution of ΔT_{Time} and ΔT_{Freq} for each point in the entire plate, respectively

nonreciprocity expends to a wider frequency range of (400, 520) and (600, 760) Hz. This broadening is attributed to the stabilization of the nonlinear bandgap caused by a sufficiently strong nonlinearity. In the range of (600, 760) Hz, $T_{\text{Time\_A2B}}$ is at least 8 dB higher than $T_{\text{Time\_B2A}}$, while in the range of (440, 520) Hz, $T_{\text{Time\_B2A}}$ is at most 5 dB higher than $T_{\text{Time\_A2B}}$. This disparity results from two nonreciprocity mechanisms along with additional factors. We examine two typical cases at 520 and 680 Hz, as illustrated in Fig. 8k, l, to delineate the nonreciprocity processes and their physical mechanisms.

4.3 Chaotic effect induced 2D nonreciprocity

At 680Hz and with $A_0 = 500$ um from A to B, the wave first enters the linear meta-plate, where it undergoes attenuation due to the LR2 bandgap. This attenuation reduces the incident amplitude upon reaching the nonlinear meta-plate, which prompts the manifestation of the LR2 bandgap. Subsequently, the wave undergoes further attenuation by the LR2 bandgap of the nonlinear meta-plate. Conversely, for B2A, the same wave first interacts with the nonlinear meta-plate, instigating chaotic wave dynamics characterized by a continuous spectrum attributable to the strong nonlinearity [11, 33]. As a result, wave energy is spread over to other frequencies before entering the linear meta-plate. As the wave travels through the linear meta-plate, only the frequency components within the LR2 bandgap are attenuated, with the remainder conserved. Consequently, $\Delta T_{\text{Time\_A2B}} = -12.83$ dB and $\Delta T_{\text{Freq\_A2B}} = -19.74$ dB. The total energy for B2A surpasses that of A2B as depicted in Fig. 9a, attributable to the conserved frequency components from the chaotic effect. Moreover, the component at 680 Hz for B2A is more than that for A2B as depicted in Fig. 9e.

This is because B2A experiences attenuation by the LR2 bandgap once, while A2B experiences the process twice. Thus, the first mechanism for nonreciprocity is the chaotic effect of the nonlinear meta-plate.

In addition to the nonreciprocity between points A and B, we further explore the nonreciprocity for the entire 2D plate. As illustrated in Fig. 9b, c, the two distributions of T_{Time} at 680 Hz in the time domain differ significantly, indicating nonreciprocal wave propagation for the entire 2D plate. A closer examination in Fig. 9d reveals that ΔT_{Time} exhibits a symmetric yet uneven distribution along the central horizontal axis. The symmetry is easily understood since the excitation point is located on the axis. However, the uneven distribution of ΔT_{Time} can be explained by the following two key factors:

1. Point excitation induces omni-directional waves: These waves experience different levels of the spatial divergence in amplitude as they encounter and travel into the nonlinear meta-plate, resulting in varying chaotic responses. For example, in Non2-Lin, a higher incident amplitude in the *X*-direction leads to stronger chaotic responses, resulting in higher transmission compared to other angles. Conversely, in Lin2Non, the linear bandgap almost entirely diminishes the wave energy, irrespective of the incidence angle of the wave. This causes ΔT_{Time} along the central horizontal line exceeding that of other orientations, as shown in Fig. 9d.
2. Reflections and refractions at multiple interfaces. Particularly at the interface containing the nonlinear meta-plate, the reflection and refraction rates are influenced by varying chaotic responses. This increases the uncertain and uneven distribution of the ΔT_{Time}.

Despite these differences, all ΔT_{Time} values are below − 10 dB threshold, with a specific $\Delta T_{\text{Time\_Lin2Non}}$ of − 15.08 dB, signifying significant nonreciprocity in this case.

Figure 9f–h illustrate that the uneven distribution of ΔT_{Freq}, similar to that of ΔT_{Time}, is also influenced by the above two factors. However, ΔT_{Time} is indicative of the reciprocity associated with the total energy, which contains all frequency components, whereas ΔT_{Freq} specifically shows the frequency component at 680 Hz. Thus, the degree and distribution of ΔT_{Freq} are different from those of ΔT_{Time}. Although $\Delta T_{\text{Freq\_Lin2Non}} = -9.04$ dB, ΔT_{Freq} can exhibit positive, negative, or zero values at different spatial locations, as shown in Fig. 9h.

Concerning this mechanism on the entire 2D plate, the wave propagation exhibits nonreciprocity in the time domain, while whether wave propagation is nonreciprocal in the frequency domain depends on the specific location. Factors like reflections and refractions at multiple interfaces, effect of wave divergence in different directions alongside the chaotic effects all influence the distribution of wave nonreciprocity within the 2D plate.

4.4 Amplitude-dependent bandgap induced 2D nonreciprocity

For a deeper understanding, we examine the wave at 520 Hz with A_0 = 500 um. This frequency lies in the passband of the linear part of the meta-plate but in the nonlinear resonant bandgap. Before reaching the nonlinear meta-plate, the same wave diverges more for A2B than for B2A. Consequently, for the former, the wave undergoes less reduction due to the amplitude-dependent band gap. As a result, $\Delta T_{\text{Time\_A2B}} = 3.4$ dB and $\Delta T_{\text{Freq\_A2B}} = 6.01$ dB, as shown in Fig. 10a, e. In contrast to the nonreciprocity observed at 680 Hz, ΔT is positive at 520 Hz, indicating a reversal in the direction of nonreciprocity. Furthermore, ΔT_{Time} and ΔT_{Freq} at 520 Hz are lower than those at 680 Hz, suggesting a lower degree of nonreciprocity based on the mechanism of amplitude-dependent bandgap. Comparing this with a 1D structure [33], we find that the wave divergence in a 2D plate accelerates the transition from NLR bandgap to LR2 bandgap, thereby weakening the degree of nonreciprocity.

Similar to the analyses conducted for 680 Hz, we analyze the 2D distribution of ΔT at 520 Hz. The nonreciprocal wave propagation for the entire 2D plate, $\Delta T_{\text{Time\_Lin2Non}} = 4.98$ dB and $\Delta T_{\text{Freq\_Lin2Non}} = 1.93$ dB, which are significantly lower than those at 680 Hz. This can be attributed again to the spatial divergence of the wave in a 2D plate which accelerates the transition from NLR bandgap to LR2 bandgap, weakening the degree of nonreciprocity.

Figure 10d, h also show an uneven distribution of ΔT_{Time} and ΔT_{Freq}, similar to those at 680Hz. However, the underlying cause of their significant fluctuations differs. These fluctuations stem from the amplitude-dependent bandgap, rather than the chaotic effect. Waves from the excitation point undergo varying levels of the spatial divergence as they propagate towards the nonlinear meta-plate, leading to different levels of attenuation by the amplitude-dependent bandgap. Additionally, reflections and refractions at multiple interfaces contribute to the uneven distributions of ΔT_{Time} and ΔT_{Freq}. The severities of reflection and refraction are particularly sensitive to the incident wave amplitude due to the amplitude-dependent nature of the bandgap, as demonstrated by the evolution of the nonlinear structures in Fig. 3.

As to the impact of this across the entire 2D plate, the efficacy of nonreciprocity in both the time and frequency domains are location dependent. The influence of the complex reflections and refractions at multiple interfaces, coupled with the orientation-

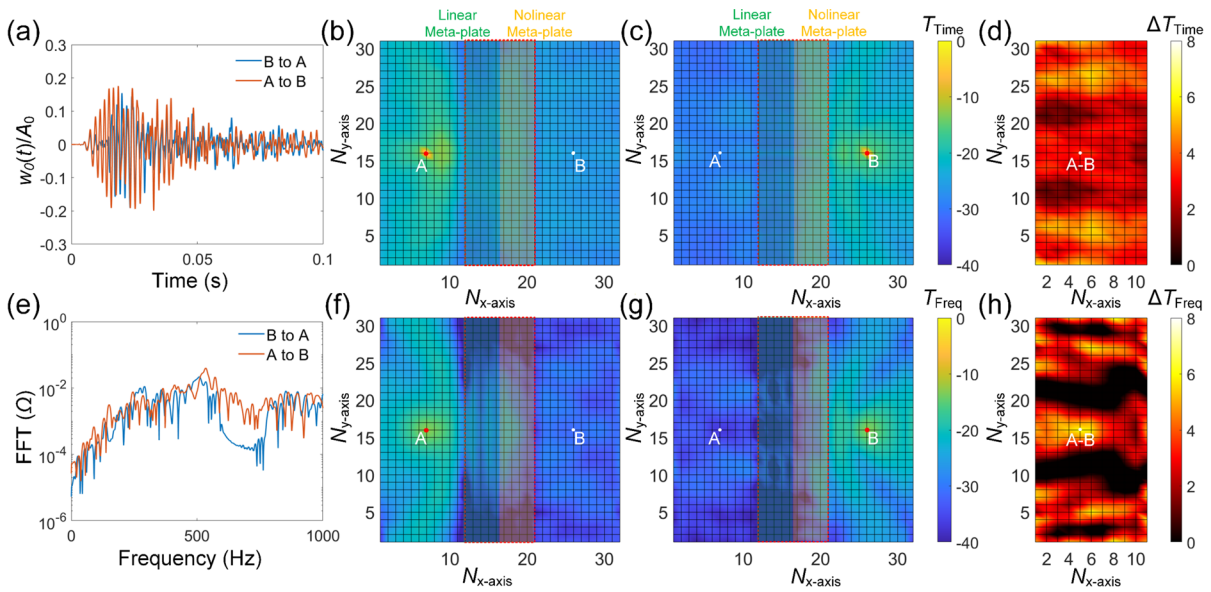

Fig. 10 Nonreciprocal wave propagation at input frequency 520 Hz in a plate with the integration of linear and nonlinear meta-plate. **a**, **e** Normalized time and frequency domains for B2A and A2B. **b**, **c** Distribution of $T_{\text{Time\_A2B}(m,\ n)}$ and $T_{\text{Time\_B2A}(m,\ n)}$ in the entire plate, respectively. **f**, **g** Distribution of $T_{\text{Freq\_A2B}(m,\ n)}$ and from $T_{\text{Freq\_B2A}}(m,\ n)$ in the entire plate, respectively. The red point indicates the point of excitation. **d**, **h** Distribution of ΔT_{Time} and ΔT_{Freq} for each point in the entire plate, respectively

dependent wave and associated with the amplitude-dependent bandgap, all together leads to the uneven distribution of nonreciprocity wave transmission within the 2D meta-plate.

5 Conclusions

NAMs have attracted considerable attention, while most theoretical studies have focused on 1D models. The properties of wave propagation in 2D NAMs (represented by plates), including the nonlinear bandgaps and nonreciprocity, are still not understood. Difficulties are from multiple aspects such as simulating the large-scale NAM models, finding all the eigenvalues and eigenvectors, displaying the evolution process and elucidating the underlying mechanisms.

This paper examines the band evolution and nonreciprocal wave propagation in a strongly nonlinear meta-plate. An accurate Shooting-Newton iteration method for solving the band structure is developed based on the nonlinear FEM model. As the amplitude is increased, the dispersion curves shift upwards, and the corresponding group velocity-frequency curves transition from single rings to multiple rings. The band evolution can be elucidated by examining the wave solution at point **R**. As predicted analytically and then confirmed numerically, the meta-plate exhibits merged local resonant modes or the engagement of a resonant mode with the Bragg mode, leading to the band degeneration. Furthermore, an equivalent method is employed to distinguish between the wave attenuation induced by bandgaps and that by spatial divergence. A nonlinear bandgap is self-adaptive to the propagation distance due to the amplitude-dependent effect. However, the bandgap-induced attenuation only prevails in a limited and localized region close to the wave generation within the 2D meta-plate. This is owing to the fact that the bandgap has a significant attenuating effect on the wave amplitudes at short distances, while the spatial divergence process accelerates the self-adaptive process. At other positions, the spatial divergence dominates the attenuation process.

Furthermore, we have integrated linear and nonlinear parts into a meta-plate to achieve nonreciprocal wave propagation. It is demonstrated that the nonreciprocal wave propagation is governed by the chaotic effect or the amplitude-dependent bandgap. The

distribution of the nonreciprocity on the 2D plate is uneven, due to the orientation-dependent wave propagation under a point input and the reflection or diffraction from multiple interfaces. Moreover, the spatial divergence in the 2D plate accelerates the transition from a local nonlinear resonant bandgap to a corresponding linear bandgap, thereby impairing the level of nonreciprocity.

In summary, we provide a novel method for the calculation of nonlinear bandgaps and introduce new phenomena and properties conducive to the control of wave propagation in strongly nonlinear 2D meta-plates. The study provides a basis for further investigations on high-dimensional NAMs, which prove to offer abundant design space to cope with various engineering applications.

Author contributions All authors contributed to the study conception and design. Material preparation, data collection was performed by Chen Gong, and analysis was performed by Chen Gong, Xin Fang and Li Cheng. The first draft of the manuscript was written by Chen Gong and all authors commented on the manuscript. All authors read and approved the final manuscript.

Funding Open access funding provided by The Hong Kong Polytechnic University. This research was funded by the Research Grant Council of the Hong Kong SAR. Xin Fang is supported by the National Natural Science Foundation of China (Projects No. 52322505 and No. 52241103) and Natural Science Fund of Hunan Province (Project No. 2023JJ10055).

Data availability The majority data has been shown in this paper. All data for this study, if not included in this published article, are available from the corresponding author on reasonable request.

Declarations

Conflict of interest The authors declare that they have no conflict of interest.

Appendix A

A.1 Finite element method and Kirchhoff–Love plate theory

Based on the finite element method and the Kirchhoff–Love plate theory [52, 53], we model the metacell of the 2D meta-plate as shown in Fig. 11, which consists of rectangular units and one resonator (red point). A convergence analysis was conducted on the number of finite elements, the results of which are presented in Fig. 11. As shown in Fig. 11a, b, the units are discretized into four rectangular plates and sixteen rectangular plates, respectively. Figure 11c, d show that the two band structures exhibit minimal discrepancy between the two discretizations, with the maximum error remaining below 0.75%. Accordingly, the former discretization with the fewer number of nodes was selected, as this reduces the computational time and barely compromise the accuracy of the results.

For modelling the meta-plate, we first establish the equation motions of the resonator and four rectangular units separately, and then assemble them to make sure the mass matrix $\mathbf{M}$ and stiffness matrix $\mathbf{K}$ of a unit cell, and finally solve the system to obtain the dispersion curves.

For the i^{th} rectangular unit, the mass matrix $\mathbf{M}_{\text{e}}$ and stiffness matrix $\mathbf{K}_{\text{e}}$ can be calculated according to the finite element method. If we do not consider the resonator in Fig. 11, there are 9 points including 27 parameters in total: $\mathbf{w}_{\text{p}i} = [w_{10}, \theta_{1\text{x}}, \theta_{1\text{y}}, \ldots, w_{90}, \theta_{9\text{x}}, \theta_{9\text{y}}]_i^{\text{T}}$. Thus, the assembly matrix $\mathbf{A}_1$, $\mathbf{A}_2$, $\mathbf{A}_3$ and $\mathbf{A}_4$ can be created to assemble the four rectangular units 1, 2, 3 and 4:

$$\mathbf{w}_{\text{p1}i} = \mathbf{A}_1\mathbf{w}_{\text{p}i},\ \mathbf{w}_{\text{p2}i} = \mathbf{A}_2\mathbf{w}_{\text{p}i},\ \mathbf{w}_{\text{p4}i} = \mathbf{A}_3\mathbf{w}_{\text{p}i},\ \mathbf{w}_{\text{p4}i} = \mathbf{A}_4\mathbf{w}_{\text{p}i} \tag{19}$$

where $\mathbf{w}_{\text{p1}i} = [w_{10}, \theta_{1\text{x}}, \theta_{1\text{y}}, w_{20}, \theta_{2\text{x}}, \theta_{2\text{y}}, w_{40}, \theta_{4\text{x}}, \theta_{4\text{y}}, w_0, w_1, w_{\text{r}}, \theta_{5\text{x}}, \theta_{5\text{y}}]_i^{\text{T}}$, $\mathbf{w}_{\text{p2}i} = [w_{20}, \theta_{2\text{x}}, \theta_{2\text{y}}, w_{30}, \theta_{3\text{x}}, \theta_{3\text{y}}, w_{60}, \theta_{6\text{x}}, \theta_{6\text{y}}, w_0, w_1, w_{\text{r}}, \theta_{5\text{x}}, \theta_{5\text{y}}]_i^{\text{T}}$, $\mathbf{w}_{\text{p3}i} = [w_{40}, \theta_{4\text{x}}, \theta_{4\text{y}}, w_{70}, \theta_{7\text{x}}, \theta_{7\text{y}}, w_{80}, \theta_{8\text{x}}, \theta_{8\text{y}}, w_0, w_1, w_{\text{r}}, \theta_{5\text{x}}, \theta_{5\text{y}}]_i^{\text{T}}$ and $\mathbf{w}_{\text{p4}i} = [w_{60}, \theta_{6\text{x}}, \theta_{6\text{y}}, w_{80}, \theta_{8\text{x}}, \theta_{8\text{y}}, w_{90}, \theta_{9\text{x}}, \theta_{9\text{y}}, w_0, w_1, w_{\text{r}}, \theta_{5\text{x}}, \theta_{5\text{y}}]_i^{\text{T}}$. After that, the mass matrix $\mathbf{M}_{\text{p}}$ and stiffness matrix $\mathbf{K}_{\text{p}}$ of the four rectangular units can be written:

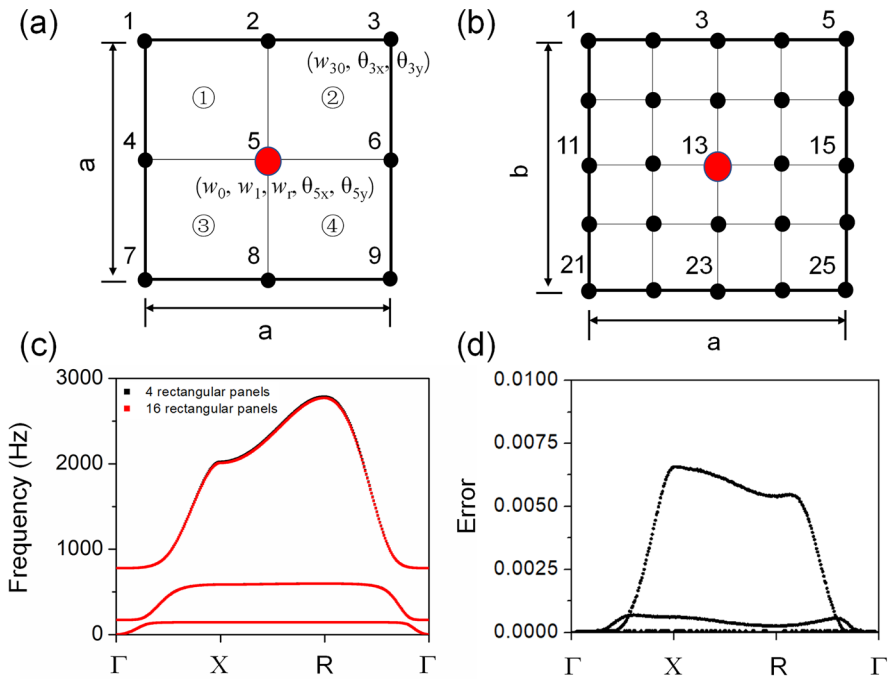

Fig. 11 A unit cell of 2D meta-plate, consisting of rectangular units and one oscillating unit (red point) **a** four rectangular units (①, ②, ③ and ④); **b** sixteen rectangular units; **c** Band structures of (**a**) and (**b**); **d** Error of (**a**)

$$\mathbf{M}_{\mathrm{p}} = \mathbf{A}_1^{\mathrm{T}}\mathbf{M}_{\mathrm{e}}\mathbf{A}_1 + \mathbf{A}_2^{\mathrm{T}}\mathbf{M}_{\mathrm{e}}\mathbf{A}_2 + \mathbf{A}_3^{\mathrm{T}}\mathbf{M}_{\mathrm{e}}\mathbf{A}_3 + \mathbf{A}_4^{\mathrm{T}}\mathbf{M}_{\mathrm{e}}\mathbf{A}_4 \tag{20}$$

$$\mathbf{K}_{\mathrm{p}} = \mathbf{A}_1^{\mathrm{T}}\mathbf{K}_{\mathrm{e}}\mathbf{A}_1 + \mathbf{A}_2^{\mathrm{T}}\mathbf{K}_{\mathrm{e}}\mathbf{A}_2 + \mathbf{A}_3^{\mathrm{T}}\mathbf{K}_{\mathrm{e}}\mathbf{A}_3 + \mathbf{A}_4^{\mathrm{T}}\mathbf{K}_{\mathrm{e}}\mathbf{A}_4 \tag{21}$$

Thus, the equation of motion for the four rectangular units writes:

$$\mathbf{M}_{\mathrm{p}}\ddot{\mathbf{w}}_{\mathrm{p}i} + \mathbf{K}_{\mathrm{p}}\ddot{\mathbf{w}}_{\mathrm{p}i} = \mathbf{0} \tag{22}$$

Next, we assemble four rectangular units and the oscillating unit. As shown in Fig. 11, the resonator locates in point 5, thus $\mathbf{w}_{\mathrm{p}i}$ adds two vectors as $\mathbf{w}_i = [w_{10}, \theta_{1x}, \theta_{1y}, \ldots, w_{40}, \theta_{4x}, \theta_{4y}, w_0, w_1, w_r, \theta_{5x}, \theta_{5y}, w_{60}, \theta_{6x}, \theta_{6y}, \ldots, w_{90}, \theta_{9x}, \theta_{9y}]_i^{\mathrm{T}}$. $\mathbf{M}_{\mathrm{p}}$ and $\mathbf{K}_{\mathrm{p}}$ expend extra 2×2 zero vectors and insert $\mathbf{M}_{\mathrm{c}}$ and $\mathbf{K}_{\mathrm{c}}$ as $\mathbf{M}$ and $\mathbf{K}$:

$$\mathbf{M} = \begin{bmatrix} \mathrm{M}_{\mathrm{p}1,1} & \cdots & \mathrm{M}_{\mathrm{p}1,13} & 0 & 0 & \mathrm{M}_{\mathrm{p}1,14} & \cdots & \mathrm{M}_{\mathrm{p}13,27} \\ \vdots & \ddots & \ldots & \vdots & \vdots & \vdots & \ddots & \vdots \\ \mathrm{M}_{\mathrm{p}13,1} & \cdots & \mathrm{M}_{\mathrm{p}13,13} & 0 & 0 & \mathrm{M}_{\mathrm{p}13,14} & \cdots & \mathrm{M}_{\mathrm{p}13,27} \\ 0 & \cdots & 0 & 0 & 0 & 0 & \cdots & 0 \\ 0 & \cdots & 0 & 0 & 0 & 0 & \cdots & 0 \\ \mathrm{M}_{\mathrm{p}14,1} & \cdots & \mathrm{M}_{\mathrm{p}14,14} & 0 & 0 & \mathrm{M}_{\mathrm{p}14,14} & \cdots & \mathrm{M}_{\mathrm{p}14,27} \\ \vdots & \ddots & \vdots & \vdots & \vdots & \vdots & \ddots & \vdots \\ \mathrm{M}_{\mathrm{p}27,1} & \cdots & \mathrm{M}_{\mathrm{p}27,14} & 0 & 0 & \mathrm{M}_{\mathrm{p}27,14} & \cdots & \mathrm{M}_{\mathrm{p}27,27} \end{bmatrix} + \begin{bmatrix} \mathbf{0}_{12\times12} & \mathbf{0} & \mathbf{0} \\ \mathbf{0} & \mathbf{M}_{\mathrm{c}} & \mathbf{0} \\ \mathbf{0} & \mathbf{0} & \mathbf{0}_{14\times14} \end{bmatrix} \tag{23}$$

$$\mathbf{K}=\begin{bmatrix} K_{p1,1} & \cdots & K_{p1,13} & 0\ 0 & K_{p1,14} & \cdots & K_{p13,27} \\ \vdots & \ddots & \cdots & \vdots\ \vdots\ \vdots & \vdots & \ddots & \vdots \\ K_{p13,1} & \cdots & K_{p13,13} & 0\ 0 & K_{p13,14} & \cdots & K_{p13,27} \\ 0 & \cdots & 0 & 0\ 0\ 0 & 0 & \cdots & 0 \\ 0 & \cdots & 0 & 0\ 0\ 0 & 0 & \cdots & 0 \\ K_{p14,1} & \cdots & K_{p14,14} & 0\ 0 & K_{p14,14} & \cdots & K_{p14,27} \\ \vdots & \ddots & \vdots & \vdots\ \vdots\ \vdots & \vdots & \ddots & \vdots \\ K_{p27,1} & \cdots & K_{p27,14} & 0\ 0 & K_{p27,14} & \cdots & K_{p27,27} \end{bmatrix} + \begin{bmatrix} \mathbf{0}_{12\times12} & \mathbf{0} & \mathbf{0} \\ \mathbf{0} & \mathbf{K}_c & \mathbf{0} \\ \mathbf{0} & \mathbf{0} & \mathbf{0}_{14\times14} \end{bmatrix} \tag{24}$$

Due to the nonlinear stiffness coefficients k_{2N} only in the oscillating unit, the nonlinear stiffness matrix of the unit cell writes:

$$\mathbf{K}_N == \begin{bmatrix} \mathbf{0}_{12\times12} & \mathbf{0} & \mathbf{0} \\ \mathbf{0} & \mathbf{k}_{Nc} & \mathbf{0} \\ \mathbf{0} & \mathbf{0} & \mathbf{0}_{14\times14} \end{bmatrix} \tag{25}$$

Thus, the equation of motion for the i^{th} metacell units writes:

$$\mathbf{M}\ddot{\mathbf{w}}_i + \mathbf{K}\mathbf{w}_i + \mathbf{K}_N\mathbf{w}_i^3 = \mathbf{0} \tag{26}$$

A.2 Bloch-Floquet theorem in 2D plate

$$(\mathbf{K} - \Omega^2\mathbf{M})\mathbf{q} + \frac{3}{4}\mathbf{K}_N\mathbf{q}^3 = \mathbf{0} \tag{27}$$

where $\mathbf{q}_i$ stands for the amplitudes of $\mathbf{w}$. According to the points in Fig. 11, $\mathbf{q}_i$ can also be divided as $\mathbf{q}_i = [\mathbf{q}_4, \mathbf{q}_8, \mathbf{q}_7, \mathbf{q}_5, \mathbf{q}_6, \mathbf{q}_2, \mathbf{q}_9, \mathbf{q}_1, \mathbf{q}_3]_i^T$, where $\mathbf{q}_{ji} = [Aw_{j0},\ A\theta_{jx},\ A\theta_{jy}]_i^T$ ($j = 1, 2, \ldots, 9,\ j \neq 5$), $\mathbf{q}_{5i} = [A_0, A_1, A_r, A\theta_{5x}, A\theta_{5y}]_i^T$ ($j = 5$), and $\Omega = 2\pi f$. Bloch-Floquet theorem can cautiously be used to deal with nonlinear systems despite some limitations [19]. Here, we will also use it to solve the above system to obtain the dispersion curves and then illustrate its limitations. According to Bloch-Floquet theorem, we can obtain the relationships of $\mathbf{q}_i$:

$$\begin{cases} \mathbf{q}_{6i} = e^{-ik\cdot a}\mathbf{q}_{4i} \\ \mathbf{q}_{2i} = e^{-ik\cdot a}\mathbf{q}_{8i} \\ \mathbf{q}_{9i} = e^{-ik\cdot a}\mathbf{q}_{7i} \\ \mathbf{q}_{1i} = e^{-ik\cdot a}\mathbf{q}_{7i} \\ \mathbf{q}_{3i} = e^{-ik\cdot 2a}\mathbf{q}_{7i} \end{cases} \tag{28}$$

Thus, we can get the equation:

$$\mathbf{q}_i = \mathbf{Z}\tilde{\mathbf{q}}_i \tag{29}$$

where $\mathbf{Z} = \begin{bmatrix} \mathbf{I}_{3\times3} & \mathbf{0} & \mathbf{0} & \mathbf{0} \\ \mathbf{0} & \mathbf{I}_{3\times3} & \mathbf{0} & \mathbf{0} \\ \mathbf{0} & \mathbf{0} & \mathbf{I}_{3\times3} & \mathbf{0} \\ \mathbf{0} & \mathbf{0} & \mathbf{0} & \mathbf{I}_{5\times5} \\ e^{-ik\cdot a}\mathbf{I}_{3\times3} & \mathbf{0} & \mathbf{0} & \mathbf{0} \\ \mathbf{0} & e^{-ik\cdot a}\mathbf{I}_{3\times3} & \mathbf{0} & \mathbf{0} \\ \mathbf{0} & \mathbf{0} & e^{-ik\cdot a}\mathbf{I}_{3\times3} & \mathbf{0} \\ \mathbf{0} & \mathbf{0} & e^{-ik\cdot a}\mathbf{I}_{3\times3} & \mathbf{0} \\ \mathbf{0} & \mathbf{0} & e^{-ik\cdot 2a}\mathbf{I}_{3\times3} & \mathbf{0} \end{bmatrix}$ and $\tilde{\mathbf{q}}_i = \begin{bmatrix} \mathbf{q}_4 \\ \mathbf{q}_8 \\ \mathbf{q}_7 \\ \mathbf{q}_5 \end{bmatrix}_i$. $\mathbf{I}_{3\times3}$ and $\mathbf{I}_{5\times5}$ represent 3×3 and 5×5 Identity matrixes, respectively.

Substituting Eq. (29) into (28) and pre-multiply the matrix $\mathbf{Z}^H$ ($\mathbf{Z}^H$ is the conjugate transpose matrix of $\mathbf{Z}$) on both sides give:

$$(\tilde{\mathbf{K}} - \Omega^2\tilde{\mathbf{M}})\tilde{\mathbf{q}}_i + \frac{3}{4}\tilde{\mathbf{K}}_N\tilde{\mathbf{q}}_i^3 = \mathbf{0} \tag{30}$$

A.3 Errors of the Shooting-Newton iteration method

This study addresses the high-dimensional nonlinear Eqs. (30) with $N = 14$. Thus, there are 14 error indicators for a given frequency after the Newton iteration. Herein, the maximum error is taken to represent the error for each frequency. Figure 12 illustrates the errors resulting from shooting all frequencies from 0 to 2000 Hz in the cases of Fig. 3. All maximum errors are below 5×10^{-10}, indicating that these solutions are convergent and persuasive.

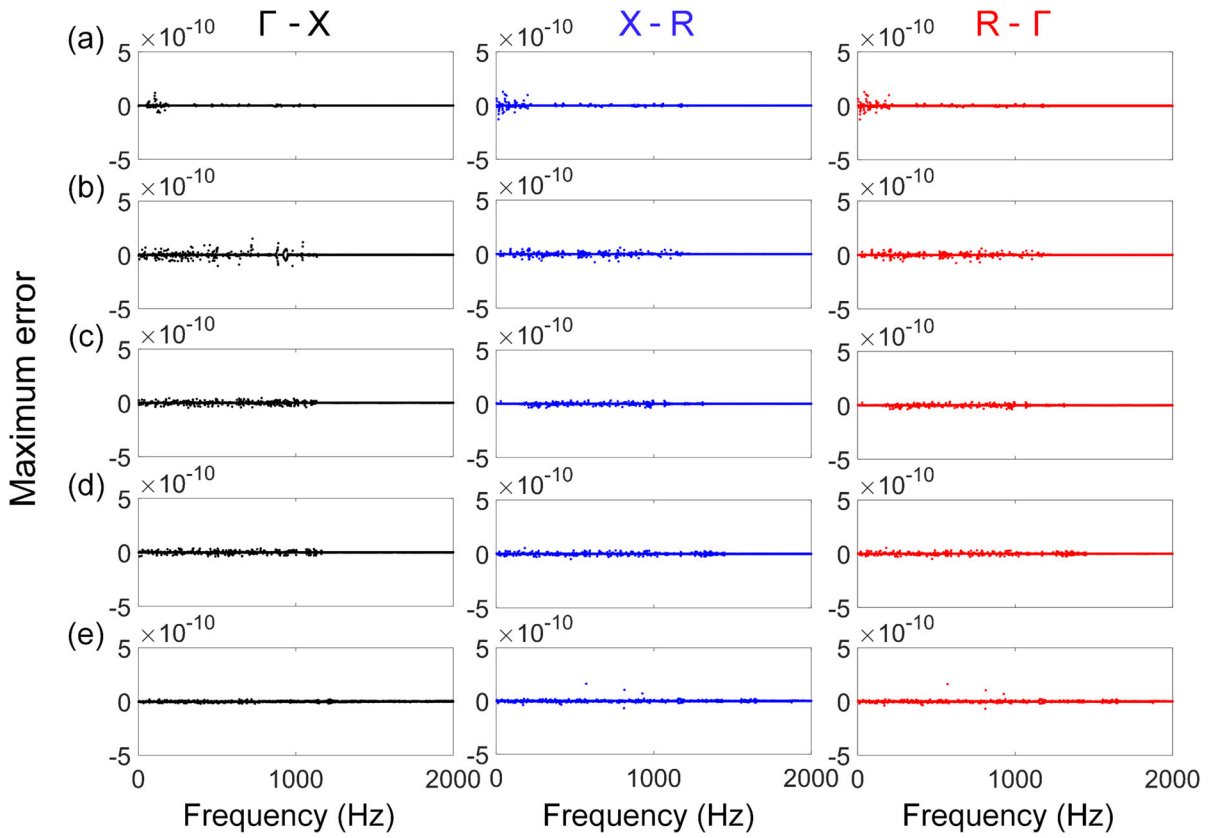

Fig. 12 The maximum error of the Shooting-Newton iteration method. **a**–**e** correspond to the cases 1–5 of Fig. 3a–e. The errors marked in Black, blue and red correspond to the maximum errors in the three boundaries (**ΓX**, **XR** and **RΓ**) of the first Brillouin zone

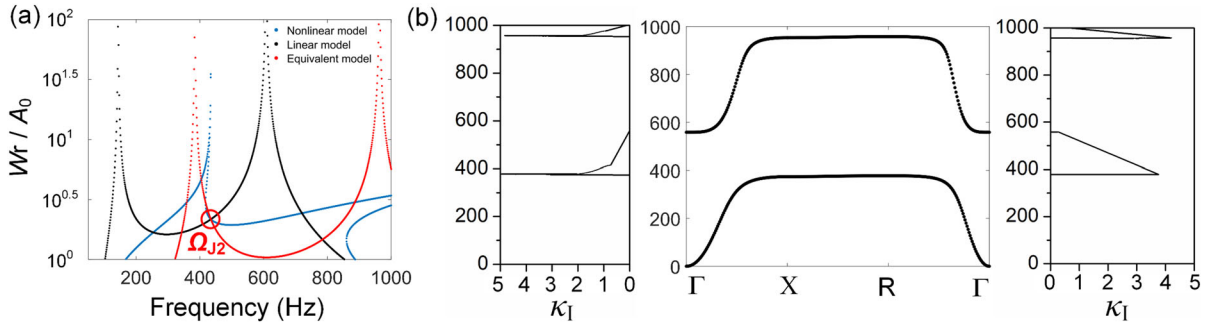

Fig. 13 **a** Transmission of local resonances. The value of w_r/A_0 is solved with Eq. (31), where curves of nonlinear model (i.e., the blue curve) are calculated with $k_{2N} = 1 \times 10^{13}$ N/m3, $A_0 = 100$ μm. The big red circle is the bifurcation point. The red curve is the equivalent linear result. **b** The real and imaginary part of the band structure when $A_0 = 100$ μm

A.4 Equivalent linearized approach

We use an equivalent linearized approach based on the bifurcation to solve the equivalent stiffness k_{2eL} between m_1 and m_2 for nonlinear models [18]. By specifying $w_{0i} = A\sin\Omega t$, $w_{1i} = Y\sin\Omega t$, $w_{2ri} = P\sin\Omega t$ in Eq. (1), and neglecting the damping effect, as well as adopting the first-order harmonic balance approach, one can solve the locally resonant responses by means of algebraic equations:

$$m_1 Y\Omega^2 = k_1(Y-A) - k_2 P - \frac{3}{4}k_{2\mathrm{N}}P^3$$
$$m_2(P+Y)\Omega^2 = k_2 P + \frac{3}{4}k_{2\mathrm{N}}P^3 + k_3(P+Y-A) \tag{31}$$

By specifying A in Eq. (31), the curve, P/A, generates a saddle-node bifurcation in the vicinity of each resonance, as illustrated with the blue curve in Fig. 13a. Ω_{J2} represents the first bifurcation frequency (the big red circle). At the bifurcation point, $P = P_{\mathrm{J2}}$. The point (Ω_{J2}, P_{J2}) is on the response curve of the equivalent linear model (the red curve), where the stiffness k_2 becomes equivalent stiffness $k_{2\mathrm{eL}}$. Therefore,

$$k_{2\mathrm{eL}} = k_2 + \frac{3}{4}k_{2\mathrm{N}}P_{\mathrm{J2}}^3 \tag{32}$$

By substituting Eq. (32) into Eq. (6) and employing the method outlined in Sect. 2.3, we can obtain the real and imaginary part of the wave number κ_{I} as shown in Fig. 13b. All errors of these solutions are below 5×10^{-10}, indicating that these solutions are convergent and persuasive.

References

1. Chen, S., Fan, Y., Fu, Q., Wu, H., Jin, Y., Zheng, J., Zhang, F.: A review of tunable acoustic metamaterials. Appl. Sci. **8**(9), 1480 (2018)
2. Liu, J., Guo, H., Wang, T.: A review of acoustic metamaterials and phononic crystals. Crystals **10**(4), 305 (2020)
3. Lu, M.-H., Feng, L., Chen, Y.-F.: Phononic crystals and acoustic metamaterials. Mater. Today **12**(12), 34–42 (2009)
4. Patil, G.U., Matlack, K.H.: Review of exploiting nonlinearity in phononic materials to enable nonlinear wave responses. Acta Mech. **233**(1), 1–46 (2022)
5. An, X., Fan, H., Zhang, C.: Elastic wave and vibration bandgaps in two-dimensional acoustic metamaterials with resonators and disorders. Wave Motion **80**, 69–81 (2018)
6. Wang, G., Yu, D., Wen, J., Liu, Y., Wen, X.: One-dimensional phononic crystals with locally resonant structures. Phys. Rev. A **327**(5–6), 512–521 (2004)
7. Xiao, Y., Wen, J., Wen, X.: Flexural wave band gaps in locally resonant thin plates with periodically attached spring–mass resonators. J. Phys. D Appl. Phys. **45**(19), 195401 (2012)
8. Xiao, Y., Wen, J., Yu, D., Wen, X.: Flexural wave propagation in beams with periodically attached vibration absorbers: band-gap behavior and band formation mechanisms. J. Sound Vib. **332**(4), 867–893 (2013)
9. Fang, X., Lacarbonara, W., Cheng, L.: Advances in nonlinear acoustic/elastic metamaterials and metastructures. Nonlinear Dyn. **6**, 1–28 (2024)
10. Fang, X., Wen, J., Bonello, B., Yin, J., Yu, D.: Ultra-low and ultra-broad-band nonlinear acoustic metamaterials. Nat. Commun. **8**(1), 1288 (2017)
11. Fang, X., Wen, J., Yin, J., Yu, D., Xiao, Y.: Broadband and tunable one-dimensional strongly nonlinear acoustic metamaterials: theoretical study. Phys. Rev. E **94**(5), 052206 (2016)
12. Fang, X., Sheng, P., Wen, J., Chen, W., Cheng, L.: A nonlinear metamaterial plate for suppressing vibration and sound radiation. Int. J. Mech. Sci. **228**, 107473 (2022)
13. Sheng, P., Fang, X., Dai, L., Yu, D., Wen, J.: Synthetical vibration reduction of the nonlinear acoustic metamaterial honeycomb sandwich plate. Mech. Syst. Signal Proc. **185**, 109774 (2023)
14. Fang, X., Wen, J., Yu, D., Yin, J.: Bridging-coupling band gaps in nonlinear acoustic metamaterials. Phys. Rev. Appl. **10**(5), 054049 (2018)
15. Hu, B., Fang, X., Cheng, L., Wen, J., Yu, D.: Attenuation of impact waves in a nonlinear acoustic metamaterial beam. Nonlinear Dyn. **111**(17), 15801–15816 (2023)
16. Zhao, C., Zhang, K., Zhao, P., Deng, Z.: Elastic wave propagation in nonlinear two-dimensional acoustic metamaterials. Nonlinear Dyn. **108**(2), 743–763 (2022)
17. Zhao, J., Zhou, H., Yi, K., Kovacic, I., Zhu, R.: Ultra-broad bandgap induced by hybrid hardening and softening nonlinearity in metastructure. Nonlinear Dyn. **111**(19), 17687–17707 (2023)
18. Fang, X., Wen, J., Benisty, H., Yu, D.: Ultrabroad acoustical limiting in nonlinear metamaterials due to adaptive-broadening band-gap effect. Phys. Rev. B **101**(10), 104304 (2020)
19. Gong, C., Fang, X., Cheng, L.: Band degeneration and evolution in nonlinear triatomic metamaterials. Nonlinear Dyn. **111**(1), 97–112 (2023)
20. Manimala, J.M., Sun, C.: Numerical investigation of amplitude-dependent dynamic response in acoustic metamaterials with nonlinear oscillators. J. Acoust. Soc. Am. **139**(6), 3365–3372 (2016)
21. Yang, B., Guo, K., Sun, J.: Towards metamaterial rods with amplitude-dependent band gaps: a superelastic alloy-based approach. Mech. Syst. Signal Proc. **166**, 108459 (2022)
22. Bukhari, M., Barry, O.: Spectro-spatial analyses of a nonlinear metamaterial with multiple nonlinear local resonators. Nonlinear Dyn. **99**(2), 1539–1560 (2020)
23. Fortunati, A., Bacigalupo, A., Lepidi, M., Arena, A., Lacarbonara, W.: Nonlinear wave propagation in locally dissipative metamaterials via Hamiltonian perturbation approach. Nonlinear Dyn. **108**(2), 765–787 (2022)
24. Manktelow, K.L., Leamy, M.J., Ruzzene, M.: Weakly nonlinear wave interactions in multi-degree of freedom periodic structures. Wave Motion **51**(6), 886–904 (2014)
25. Narisetti, R.K., Leamy, M.J., Ruzzene, M.: A perturbation approach for predicting wave propagation in one-dimensional nonlinear periodic structures. J. Sound Vib. **132**, 3 (2010)
26. Narisetti, R.K., Ruzzene, M., Leamy, M.J.: Study of wave propagation in strongly nonlinear periodic lattices using a harmonic balance approach. Wave Motion **49**(2), 394–410 (2012)

27. Fang, X., Wen, J., Yin, J., Yu, D.: Wave propagation in nonlinear metamaterial multi-atomic chains based on homotopy method. AIP Adv. **6**(12), 121706 (2016)
28. Fronk, M.D., Fang, L., Packo, P., Leamy, M.J.: Elastic wave propagation in weakly nonlinear media and metamaterials: a review of recent developments. Nonlinear Dyn. **111**(12), 10709–10741 (2023)
29. Gao, M., Wu, Z., Wen, Z.: Effective negative mass nonlinear acoustic metamaterial with pure cubic oscillator. Adv. Civ. Eng. **2018**, 1–15 (2018)
30. Wu, Z., Zheng, Y., Wang, K.: Metastable modular metastructures for on-demand reconfiguration of band structures and nonreciprocal wave propagation. Phys. Rev. E **97**(2), 022209 (2018)
31. Bae, M.H., Oh, J.H.: Amplitude-induced bandgap: new type of bandgap for nonlinear elastic metamaterials. J. Mech. Phys. Solids **139**, 103930 (2020)
32. Cabaret, J., Tournat, V., Béquin, P.: Amplitude-dependent phononic processes in a diatomic granular chain in the weakly nonlinear regime. Phys. Rev. E **86**(4), 041305 (2012)
33. Fang, X., Wen, J., Cheng, L., Li, B.: Bidirectional elastic diode with frequency-preserved nonreciprocity. Phys. Rev. Appl. **15**(5), 054022 (2021)
34. Maznev, A., Every, A., Wright, O.: Reciprocity in reflection and transmission: what is a 'phonon diode'? Wave Motion **50**(4), 776–784 (2013)
35. Nassar, H., Yousefzadeh, B., Fleury, R., Ruzzene, M., Alù, A., Daraio, C., et al.: Nonreciprocity in acoustic and elastic materials. Nat. Rev. Mater. **5**(9), 667–685 (2020)
36. Rasmussen, C., Quan, L., Alù, A.: Acoustic nonreciprocity. J. Appl. Phys. **129**, 21 (2021)
37. Wu, G., Long, Y., Ren, J.: Asymmetric nonlinear system is not sufficient for a nonreciprocal wave diode. Phys. Rev. B **97**(20), 205423 (2018)
38. Gong, C., Fang, X., Cheng, L.: Multi-state dynamics and model similarity of a vibro-impact nonlinear system. Int. J. Nonlin. Mech. **8**, 104765 (2024)
39. Farzbod, F., Michael, J.L.: Analysis of Bloch's method and the propagation technique in periodic structures. J. Vib. Acoust. **133**(3), 03101 (2011)
40. Shen, Y., Lacarbonara, W.: Nonlinearity enhanced wave bandgaps in metamaterial honeycombs embedding spider web-like resonators. J. Sound Vib. **562**, 11782 (2023)
41. Osborne, M.R.: On shooting methods for boundary value problems. J. Math. Anal. Appl. **27**(2), 417–433 (1969)
42. Ribeiro, P.: Non-linear forced vibrations of thin/thick beams and plates by the finite element and shooting methods. Comput. Struct. **82**(17–19), 1413–1423 (2004)
43. Sim, Y.C., Leng, S.B., Subramaniam, V.: A combined genetic algorithms-shooting method approach to solving optimal control problems. Int. J. Syst. Sci. **31**(1), 83–89 (2000)
44. Victor, G.: Structural Health Monitoring with Piezoelectric Wafer Active Sensors, vol. 5. Elsevier, Amsterdam (2014)
45. Liang, B., Guo, X., Tu, J., Zhang, D., Cheng, J.: An acoustic rectifier. Nat. Mater. **9**(12), 989–992 (2010)
46. Grinberg, I., Vakakis, A.F., Gendelman, O.V.: Acoustic diode: wave non-reciprocity in nonlinearly coupled waveguides. Wave Motion **83**, 49–66 (2018)
47. Gliozzi, A.S., Miniaci, M., Krushynska, A.O., Morvan, B., Scalerandi, M., Pugno, N.M., et al.: Proof of concept of a frequency-preserving and time-invariant metamaterial-based nonlinear acoustic diode. Sci. Rep. **9**(1), 9560 (2019)
48. Boechler, N., Theocharis, G., Daraio, C.: Bifurcation-based acoustic switching and rectification. Nat. Mater. **10**(9), 665–668 (2011)
49. Darabi, A., Fang, L., Mojahed, A., Fronk, M.D., Vakakis, A.F., Leamy, M.J.: Broadband passive nonlinear acoustic diode. Phys. Rev. B **99**(21), 214305 (2019)
50. Mojahed, A., Bunyan, J., Tawfick, S., Vakakis, A.F.: Tunable acoustic nonreciprocity in strongly nonlinear waveguides with asymmetry. Phys. Rev. Appl. **12**(3), 034033 (2019)
51. Lu, Z., Norris, A.N.: Nonreciprocal and directional wave propagation in a two-dimensional lattice with bilinear properties. Nonlinear Dyn. **106**, 2449–2463 (2021)
52. Dhatt, G., Lefrançois, E., Touzot, G.: Finite Element Method. Wiley, Berlin (2012)
53. Genta, G.: Vibration Dynamics and Control. Springer, New York (2009)